Nanoscale Advances

ROYAL SOCIETY OF CHEMISTRY

PAPER

View Article Online
View Journal

Cite this: DOI: 10.1039/d6na00081a

Nanostructured ZIF-67/$LaFeO_3$ p–n heterojunction interface for amplified cefotaxime sensing & intensified photo-Fenton degradation

Monalisa Samal,[a] Dakshita Snud Sharma,[b] Dharitri Rath,[b] Jagannath Panda,[c] P. Ganga Raju Achary[a] and Binita Nanda*[a]

The efficient removal and detection of antibiotic contaminants without generating hazardous byproducts remain critical challenges in environmental chemistry. Herein, a ZIF-67/$LaFeO_3$ nanocomposite with a high specific surface area (1082.94 m^2 g^{-1}) is constructed to function as a dual mode photocatalyst and electrochemical sensor for cefotaxime (CFX). Benefiting from a synergistic type-II p–n heterojunction, the composite exhibits rapid visible light driven photocatalytic degradation of CFX in the presence of hydrogen peroxide (H_2O_2), achieving 90.1% removal within 10 min with an apparent rate constant (K_{app}) of 0.1014 min^{-1}, markedly outperforming pristine ZIF-67 and $LaFeO_3$. When integrated onto a screen-printed carbon electrode, the ZIF-67/$LaFeO_3$ electrode demonstrates sensitive electrochemical detection of CFX with a limit of detection of 3.41 ppm and a limit of quantification of 10.1 ppm at pH 6 and 40 ppm cefotaxime (CFX) concentration. Electrochemical impedance spectroscopy (EIS) reveals enhanced charge separation efficiency and reduced interfacial charge transfer resistance upon $LaFeO_3$ integration. Degradation intermediates and plausible reaction pathways are identified by high-resolution mass spectroscopy (HR-MS). This study demonstrates the rational design of a heterostructure MOF-based system for integrated antibiotic sensing and wastewater remediation.

Received 31st January 2026
Accepted 6th March 2026

DOI: 10.1039/d6na00081a

rsc.li/nanoscale-advances

1. Introduction

Increasing inhabitant numbers have led to several developments in business and industry.[1] Nevertheless, although urbanization is necessary for human survival, its rapid acceleration has increased the level of pollutants and environmental illnesses by elevating the concentration of contaminants in water, including dyes, heavy metals, pesticides, and antibiotics, which damage ecosystems and seriously impair human health. Hence water contamination is becoming a major global concern.[2] Antibiotics are regarded as novel and persistent pollutants among the many contaminants found in the aquatic environment.[3,4] Among antibiotics, cefotaxime (CFX), a member of the β-lactam group, is particularly concerning in water and humans due to its high antibiotic activity, resistance induction, and potential toxicity. CFX is a broad-spectrum cephalosporin antibiotic used to treat a wide range of infections caused by both Gram-positive and Gram-negative bacteria. Despite the low environmental concentrations and low toxicity of CFX, a greater concern is that its metabolized by products enter soils and water systems, promoting the proliferation of antibiotic-resistant bacteria and resistance genes.[5] Furthermore, despite its biodegradability, CFX cannot be efficiently eliminated by traditional wastewater treatment methods.[6] Thus, alternative approaches must be developed to address antibiotic contamination.

Organic pollutants have been removed using a range of remediation approaches, including physical, biological, and commonly used chemical treatments such as UV irradiation, Fenton reactions, and ozonation.[7,8] Although commonly employed, traditional treatment methods have high energy requirements and pose a risk of secondary contamination. In contrast, solar-driven semiconductor photocatalysis offers an affordable, sustainable, and environmentally benign option for environmental rehabilitation.[9] Among these advanced oxidation processes (AOPs), the photo-Fenton reaction increases the efficiency of pollutant degradation by producing highly oxidizing hydroxyl ($^{\bullet}OH$) radicals using hydrogen peroxide (H_2O_2) and iron salts.[10,11] The photo-Fenton reaction produces $^{\bullet}OH$ radicals by ferrous ion (Fe^{2+}) mediated H_2O_2 breakdown, and light irradiation increases the production of $^{\bullet}OH$ through ferric ion (Fe^{3+}) reduction and H_2O_2 photolysis, allowing for the effective destruction of organic pollutants.[12,13] However, conventional photo-Fenton systems frequently suffer from drawbacks such as high catalyst costs, poor stability, and rapid

[a]Department of Chemistry, Faculty of Engineering and Technology (ITER), Siksha O Anusandhan (Deemed to be) University, Bhubaneswar, Odisha, India, 751 030. E-mail: binitananda@soa.ac.in

[b]Department of Chemical Engineering, Indian Institute of Technology Jammu (IIT), Jagti, Jammu – 181 221, Jammu and Kashmir, India

[c]Department of Chemistry, NIST University, Institute Park, Pallur Hills, Berhampur, India

catalyst deactivation.[14] To overcome these limitations, the combination of metal–organic frameworks (MOFs) and iron oxide-based catalysts has garnered significant attention.[15]

The potential of MOFs as adsorbents and catalysts has attracted significant attention due to their high surface area, large pore size, tuneability, well-defined nanometre-scale cavities, and chemical tailorability.[16] In MOFs, the bridging ligands often serve as light-capturing antennae. This energy absorption can initiate a phenomenon known as ligand-to-metal charge transfer (LMCT).[17] Alternatively, light may be directly absorbed by the metal clusters themselves.[18] Zeolitic imidazolate frameworks (ZIFs), a well-known subclass of MOFs, combine the advantageous qualities of both MOFs and zeolites, including high porosity, cage-like cavities, adjustable pore shapes, particular functions, and remarkable stability. These properties have led to exciting opportunities for applications in immobilized enzymes, gas adsorption and separation, energy storage, sensor detection, and effective catalysis.[19] Among ZIFs, ZIF-67 is a promising candidate for enhanced photocatalytic performance due to its high specific surface area, low volatility, appropriate pore size, excellent photocatalytic reaction in visible light, high thermal stability, strong chemical stability, and a conductivity band of 1.9 eV.[20]

Furthermore, owing to its non-toxic nature, high stability, and narrow band gap, $LaFeO_3$ shows promise as a visible light photocatalyst. Additionally, it exhibits a distinctive ABO_3-type perovskite structure, in which "A" represents a rare earth metal and "B" denotes a transition metal. Owing to its unique structure and intrinsic properties, the perovskite structure has attracted considerable scientific attention.[21] Current applications include solid oxide fuel cells, chemical sensors, catalysts, and magnetic and electrode materials.[22,23] Recent reports have shown that nanostructured and hybrid materials significantly enhance electrochemical sensing by improving interfacial charge transfer and electrocatalytic activity. Alhazmi *et al.* and Imran *et al.* demonstrated adsorption-assisted and irreversible electrochemical oxidation of pharmaceutical and β-lactam antibiotic molecules using nanomaterial-based platforms, while mixed metal oxide composites further benefit from synergistic metal–metal interactions. These studies provide a relevant framework for employing the ZIF-67/$LaFeO_3$ MOF–perovskite hybrid as an electrocatalytic sensing interface.[24–26] The remarkable oxygen mobility and structural stability associated with multiple oxidation states in perovskites contribute to their catalytic flexibility.[23] The effectiveness of transition metal-based perovskites in accelerating the breakdown of H_2O_2 has drawn increasing interest due to their use as catalytic components in carbon-based electrodes, especially those with compositions such as $LaFeO_3$, $LaMnO_3$, and $LaCrO_3$.[27] The concentration of highly oxidized transition metal species (such as Ni^{3+} and Fe^{4+}) and the degree of oxygen non-stoichiometry are important factors that regulate the breakdown of H_2O_2, according to these research studies, in addition to metal composition.[28] $LaFeO_3$ functions as a heterogeneous catalyst that, when exposed to UV radiation and H_2O_2, promotes the conversion of Fe^{3+} to Fe^{2+}. This procedure is crucial for producing hydroxyl radicals (˙OH), potent oxidants that may break down organic contaminants. Hydroxyl radicals (˙OH) and hydroxide ions (OH^-) are produced when H_2O_2 is reduced by the Fe^{2+} ion produced from $LaFeO_3$ given in eqn (1) and (2). These very reactive radicals play a crucial role in the breakdown of organic contaminants.

$$Fe^{3+} + e^- \rightarrow Fe^{2+} \quad (1)$$

$$Fe^{2+} + H_2O_2 \rightarrow Fe^{3+} + OH^- + OH^{\cdot} \quad (2)$$

This study investigates the sol–gel method, a simple and widely used synthesis process known for its efficacy and versatility, which enables controlled synthesis of the ZIF-67/$LaFeO_3$ nanocomposite, resulting in better dispersion of the catalyst and enhancing its stability and reusability. The study further explores the potential of the ZIF-67/$LaFeO_3$ nanocomposite in CFX photo-Fenton photocatalysis, emphasizing its effectiveness, rates of degradation, and underlying processes. The hybrid catalyst offers a viable approach to remediate pharmaceutical pollutants in wastewater by encouraging the production of hydroxyl radicals under UV irradiation. These radicals aid in the breakdown of cefotaxime and other organic contaminants. To develop advanced and environmentally sustainable photocatalytic systems, this approach highlights the advantages of combining MOFs with iron oxide-based catalysts.

2. Experimental section

2.1 Materials

Cobalt nitrate hexahydrate (99%, SRL), 2-methylimidazole (99%, SRL), sodium hydroxide pellets (Merck), silver nitrate (99.5%, SRL), ethanol (Merck), methanol (Merck), cefotaxime salt ($C_{16}H_{17}N_5O_7S_2$, 98%, Himedia), iron nitrate hexahydrate (99%, SRL), lanthanum nitrate hexahydrate (99%, SRL), and citric acid ($C_6H_8O_7$) (98%, Himedia). Analytical grade (AR) reagents were used throughout this investigation, ensuring high purity without the need for further purification.

2.2 Synthesis methods

The detailed synthesis procedures of ZIF-67, $LaFeO_3$, and the composite ZIF-67/$LaFeO_3$ are given in the SI. The reaction mechanistic pathway is explained below.

2.2.1 Reaction mechanism of ZIF-67. ZIF-67 is produced by combining imidazole ligands ($C_3H_3N_2^-$) with Co^{2+} ions. In a network structure, the imidazole ligands function as bridging ligands and the cobalt ions as nodes or metal centres. The nucleation of tiny clusters and their subsequent development into bigger crystalline formations are the first steps in the process. Temperature (60 °C) and the solvent (methanol) are important factors in regulating the size of the crystals that form as well as the pace of nucleation.[29] A homogeneous reaction mixture is produced when the solvent, in this case methanol, aids in the dissolution of the imidazole ligands and the cobalt salt (cobalt nitrate hexahydrate).[30] The form and rate of crystallization of the resultant ZIF-67 crystals can also be affected by the solvent. As shown in Fig. 1a, the imidazole ligands

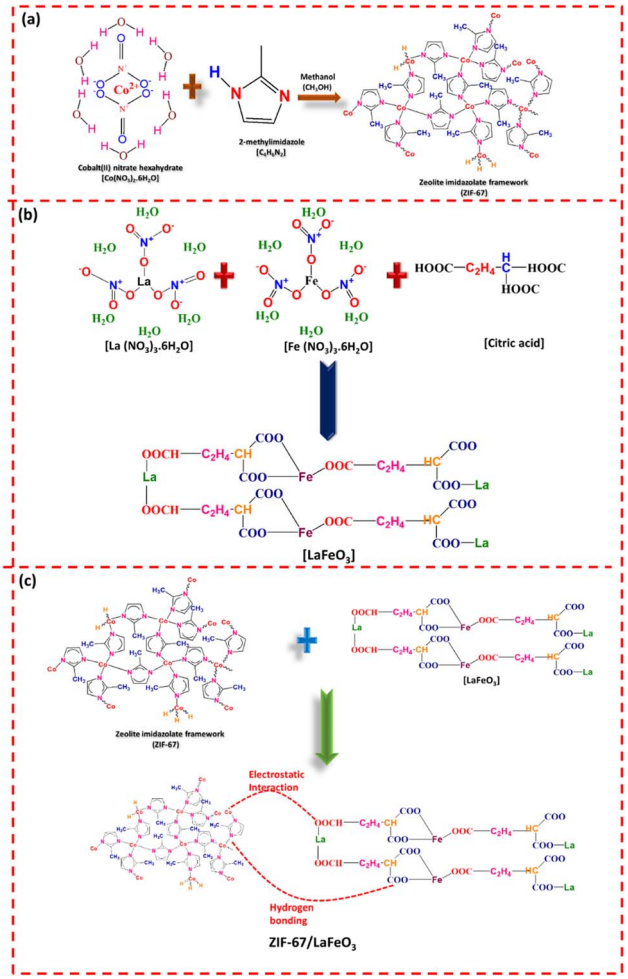

Fig. 1 Synthesis of (a) ZIF-67, (b) $LaFeO_3$, and (c) ZIF-67/$LaFeO_3$.

coordinate with Co^{2+} ions to form a tetrahedral coordination geometry around each cobalt centre. Subsequently, these tetrahedrally coordinated cobalt ions connect with adjacent imidazole groups to form a three-dimensional network structure. In the first step cobalt nitrate hexahydrate dissociates in methanol, releasing Co^{2+} ions and nitrate ions (NO_3^-), as given in eqn (3).

$$Co(NO_3)_2\cdot 6H_2O \rightarrow Co^{2+} + 2NO_3^- + 6H_2O \quad (3)$$

After that, in the second phase, the imidazole molecules ($C_3H_3N_2$) coordinate with the cobalt ions, forming a metal–ligand complex, as shown in eqn (4).

$$Co^{2+} + C_3H_3N_2 \rightarrow [Co(C_3H_3N_2)_2]^{2+} \quad (4)$$

When the process is heated to 60 °C, the cobalt–imidazolate complexes come together to form the ZIF-67 framework, which is a 3D network (eqn (5) and (6)).

$$[Co(C_3H_3N_2)_2] + \text{ZIF-67 framework} \quad (5)$$

$$Co(NO_3)_2\cdot 6H_2O + 2C_3H_3N_2 \rightarrow \text{ZIF-67} \quad (6)$$

2.2.2 Reaction mechanism of $LaFeO_3$. Lanthanum nitrate hexahydrate [La $(NO_3)_3\cdot 6H_2O$] and iron nitrate hexahydrate [Fe $(NO_3)_3\cdot 6H_2O$] were dissolved in distilled water to form an aqueous solution. Citric acid ($C_6H_8O_7$) was added as a chelating agent to regulate the coordination of metal ions and encourage uniform mixing.[31] Maintaining the pH of the solution at 7 helps to guarantee its stability and stop undesired precipitates from forming. Upon heating to 70 °C, the solution undergoes dehydration and condensation, resulting in the formation of a thick gel.[32] By creating stable complexes with both La^{2+} and Fe^{2+} ions, citric acid functions as a complexing agent and aids in regulating the final homogeneity of the product.[33] After that, it is dried at 90 °C, which causes the water to evaporate and the gel to solidify into a more rigid structure. The dried gel is subsequently calcined in air at 500 °C to obtain the final $LaFeO_3$ product, as illustrated in Fig. 1b. During the calcination process, organic components break down and crystallize, and the perovskite $LaFeO_3$ structure is formed.

The metal ions separate when distilled water is added to lanthanum nitrate and iron nitrate hexahydrate. Now, these metal ions (Fe^{3+} and La^{3+}) can react with citric acid without restriction.

$$La(NO_3)_3\cdot 6H_2O \rightarrow La^{3+} + 3NO_3^- + 6H_2O \quad (7)$$

$$Fe(NO_3)_3\cdot 6H_2O \rightarrow Fe^{3+} + 3NO_3^- + 6H_2O \quad (8)$$

The metal ions La^{3+} and Fe^{3+} form stable complexes with citric acid ($C_6H_8O_7$). The carboxylic group (–COOH) of citric acid works in coordination with the metal ions to stabilize the solution and stop the metal ions from precipitating prior to the gelation process.

$$La^{3+} + C_6H_8O_7 \rightarrow [La(C_6H_8O_7)]^{3+} \quad (9)$$

$$Fe^{3+} + C_6H_8O_7 \rightarrow [Fe(C_6H_8O_7)]^{3+} \quad (10)$$

Oxidation and breakdown of the organic ligands (from citric acid) produce gases such as CO_2 and H_2O. The perovskite structure of $LaFeO_3$ is formed through the reaction between La^{3+} and Fe^{3+} metal ions.

$$[La(C_6H_8O_7)]^{3+} + [Fe(C_6H_8O_7)]^{3+} \rightarrow LaFeO_3 + CO_2 + H_2O \quad (11)$$

2.2.3 Reaction mechanism of ZIF-67/$LaFeO_3$. The ZIF-67/$LaFeO_3$ nanocomposite is a hybrid material that integrates the catalytic and semiconducting properties of the metal oxide $LaFeO_3$ with the highly porous framework of the metal–organic framework ZIF-67. During synthesis, cobalt nitrate hexahydrate was dissolved in methanol, and $LaFeO_3$ powder was dispersed into this solution. The mixture was sonicated for 30 min, which enhanced the dispersion of $LaFeO_3$ particles and promoted the adsorption of Co^{2+} ions onto the $LaFeO_3$ surface.[15] In methanol, Co^{2+} ions are readily solvated and remain in solution, whereas

$LaFeO_3$ does not dissolve and instead exists as finely dispersed solid particles. Sonication improves the interaction between the $LaFeO_3$ surface and Co^{2+} ions by preventing particle agglomeration and increasing the available surface area, thereby facilitating the subsequent formation of the ZIF-67 framework on $LaFeO_3$.

$$Co(NO_3)_2 \cdot 6H_2O \rightarrow Co^{2+} + 2NO_3^- + 6H_2O \quad (12)$$

2-Methylimidazole was prepared in a different solution in methanol. To the $Co^{2+}/LaFeO_3$ dispersion, this ligand solution was added dropwise. This is a self-assembly reaction that is fuelled by coordination. Using four nitrogen atoms from four 2-methylomidazole molecules, each Co^{2+} ion coordinates tetrahedrally. The reaction in methanol takes place at room temperature or at a little higher temperature.

$$Co^{2+} + 2C_3H_3N_2 \rightarrow [Co(C_3H_3N_2)_2] \rightarrow \text{ZIF-67} \quad (13)$$

The surface of $LaFeO_3$ serves as a heterogeneous nucleation location. ZIF-67 nucleation is started immediately on the $LaFeO_3$ particles when Co^{2+} ions close to the surface align with $C_3H_3N_2$ ligands as shown in Fig. 1c. ZIF-67 crystals connected to $LaFeO_3$ grow as a result of this.

$$LaFeO_3 + Co^{2+} + 2C_3H_3N_2 \rightarrow LaFeO_3/\text{ZIF-67} \quad (14)$$

2.3 Electrochemical properties

To fabricate the working electrode, the screen-printed carbon electrode (SPCE) was first cleaned thoroughly with deionized (DI) water. Subsequently, 1 mg of the material was dispersed in 1 mL of dimethylformamide (DMF), and the suspension was sonicated for 1–2 h to obtain a homogeneous dispersion. An aliquot of 4 μL of the prepared dispersion was drop-cast onto the working electrode surface and allowed to dry naturally at room temperature. Electrochemical characterization was performed using a Metrohm DropSens potentiostat through cyclic voltammetry (CV) and electrochemical impedance spectroscopy (EIS). For these measurements, the SPCE was covered with a 5 mM ferro/ferricyanide ($[Fe(CN)_6]^{3-}/[Fe(CN)_6]^{4-}$) solution prepared in 1 M KCl as the supporting electrolyte.

2.4 Characterization

X-ray diffraction (XRD), Fourier transform infrared (FTIR) spectroscopy, Ultraviolet-Visible Diffuse Reflectance Spectroscopy (UV-Vis DRS), X-ray Photoelectron Spectroscopy (XPS), High-Resolution Transmission Electron Microscopy (HR-TEM), Brunauer–Emmett–Teller (BET) analysis and Field Emission Scanning Electron Microscopy (FE-SEM) were used to characterize the samples. A Rigaku Miniflex X-ray diffractometer was used to investigate the crystal structure of the samples utilizing a CuKα radiation source ($\lambda = 1.5406$ Å) at 40 kV and 15 Ma in the Bragg diffraction angle range of 10 °C to 90 °C. The surface morphology was obtained by field emission scanning electron microscopy (FESEM JSM 7900F, JEOL) and high-resolution electron microscopy (NEOARM/JEM-ARM200F JEOL). The surface morphology of the sample was examined using energy dispersive spectrum analysis (EDS), N_2 adsorption/desorption isotherms were used to compute the specific surface areas and pore size distributions using the Brunauer–Emmett–Teller technique (Quanta chrome Auto sorb) at liquid nitrogen temperature (70 K). A Jasco FT/IR4600LE was used to measure the molecular vibrations of the samples using Fourier transform infrared spectroscopy in order to assess the chemical composition and physical state of the entire sample in the 400–4000 cm^{-1} range. The samples were subjected to UV-visible diffuse reflectance spectroscopy in the 200–800 nm range using a Jasco-750 UV-Vis spectrophotometer. X-ray photoelectron spectroscopy spectra (Thermo Scientific NEXA surface analyzer) were used to investigate the ZIF-67/$LaFeO_3$ surface elements using an X-Ray003 100 μm – FG ON (100 μm) X-ray source.

For additional details, refer to the SI.

3. Results and discussion

3.1 Structural and textural analysis

XRD analysis was performed to investigate the crystal structures of ZIF-67, $LaFeO_3$, and the ZIF-67/$LaFeO_3$ nanocomposite. The crystalline phases were analysed using a Rigaku diffractometer equipped with CuKα radiation ($\lambda = 1.5406$ Å). XRD data were collected over a 2θ range of 10–90 °C. As shown in Fig. 2a, ZIF-67 exhibited characteristic diffraction peaks at 2θ values of 9.40°, 13.36°, 15.60°, 19.0°, 21.21°, and 20.90°, corresponding to the (011), (002), (112), (022), (013), and (222) crystal planes, respectively. These diffraction peaks closely match those reported in the JCPDS card no. 96-224-3192,[34] confirming the monoclinic crystal structure of the synthesized ZIF-67. The XRD pattern of $LaFeO_3$ displayed distinct diffraction peaks at 2θ values of 22.60°, 32.30°, 39.80°, 46.30°, 52.00°, 57.40°, 67.40°, and 76.80°, which correspond to the (100), (110), (111), (200), (210), (211), (220), and (310) planes, respectively. These peaks are in good agreement with JCPDS no. 01-075-0541, confirming the successful synthesis of phase-pure $LaFeO_3$ with a cubic crystal structure. In the XRD pattern of the ZIF-67/$LaFeO_3$ nanocomposite, most of the distinctive peaks of ZIF-67 disappeared, while a few primary peaks at 13.36° 15.60° and 19.00°, were retained with significantly reduced intensity and a slight shift toward lower angles. This behaviour indicates strong interaction between ZIF-67 and $LaFeO_3$. Moreover, diffraction peaks corresponding to both ZIF-67 and $LaFeO_3$ were observed in the composite pattern, confirming successful formation of the composite.[35] The diffraction pattern of ZIF-67/$LaFeO_3$ matches well with JCPDS card no. 01-089-8280, indicating an orthorhombic crystal structure.

The average crystallite size (L) of the samples was estimated using the Scherrer equation (eqn (15)):[20]

$$L = K\lambda/\beta \cos\theta \quad (15)$$

where λ is the X-ray photon wavelength (0.15418), K is often assumed to be 0.89, β is the full width at half maximum, and L is

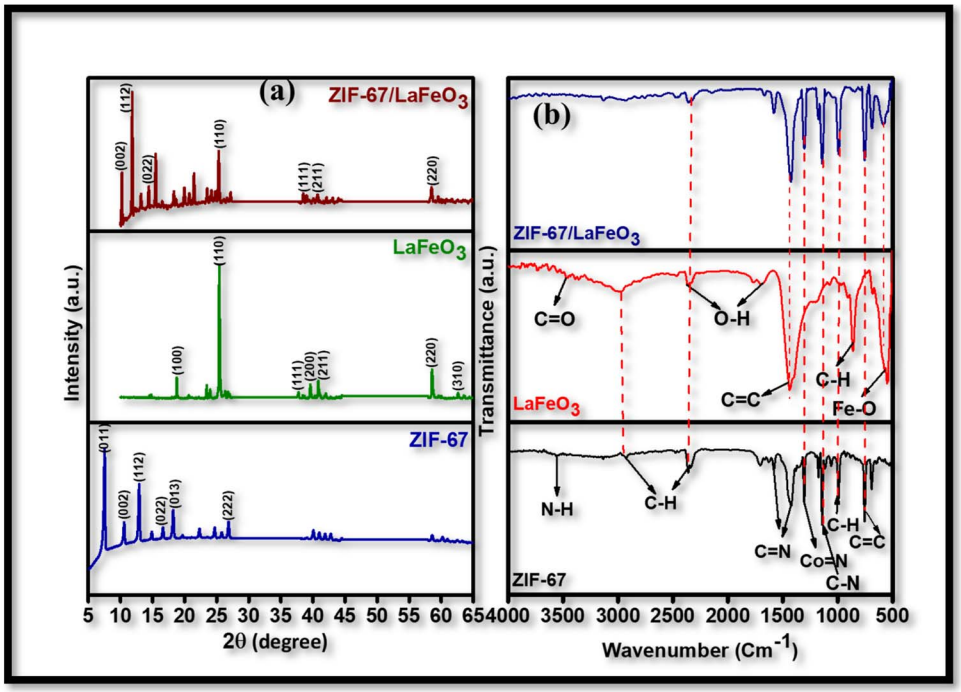

Fig. 2 (a) XRD patterns of ZIF-67, $LaFeO_3$, and ZIF-67/$LaFeO_3$. (b) FT-IR spectra of ZIF-67, $LaFeO_3$, and ZIF-67/$LaFeO_3$.

the crystalline size in nm.[36] According to calculations, the typical crystallite diameters for ZIF-67, $LaFeO_3$, and ZIF-67/$LaFeO_3$ were around 68.5 nm, 32.43 nm, and 46.8 nm respectively. Broadening of the diffraction peaks (β) was observed with increasing $LaFeO_3$ content, which is inversely related to the average crystallite size, consistent with the Scherrer analysis.

Bragg's equation (eqn (16)) was used to determine the interplanar spacing (d) between ZIF-67 and $LaFeO_3$:[37]

$$d = \lambda/2 \sin\theta \quad (16)$$

where d is the interplanar distance in nanometres between layers, λ is the wavelength of X-ray radiation (0.15418 nm), and θ is Bragg's angle. ZIF-67 and $LaFeO_3$ were separated by 0.202 nm.

FTIR was further used to confirm the structural integrity and functional groups present in the materials, while XRD validated their crystalline structure. The FT-IR spectra of ZIF-67, $LaFeO_3$, and ZIF-67/$LaFeO_3$ are presented in Fig. 2b and were recorded in the wavenumber range of 500–4000 cm^{-1}. In the FTIR spectrum of ZIF-67, the bands observed at 2942.0 and 2337.1 cm^{-1} correspond to aliphatic C–H stretching vibration originating from the methylimidazole ligand. The peaks at 1554.0 and 1428.2 cm^{-1} are attributed to C=N stretching vibrations of the imidazole ring, while the peak at 757.1 cm^{-1} corresponds to the C=C vibrations.[38] Furthermore, the peak at 3569.1 cm^{-1} is associated with the N–H group, and the peak at 1303.0 cm^{-1} is assigned to the Co=N bond. For $LaFeO_3$, characteristic absorption bands were observed at 1436.1, 1687.0, 2330.4, 3466.3, 543.1, and 853.2 cm^{-1}. The distinctive band at 543 cm^{-1} corresponds to Fe–O stretching vibrations,[39] confirming the formation of the perovskite structure, as this band typically appears in the 500–700 cm^{-1} range. The peaks at 1687.0 and 2330.4 cm^{-1} are attributed to asymmetric carboxyl stretching vibrations, while the peak at 3466.3 cm^{-1} corresponds to asymmetric O–H stretching vibrations.[40] The FTIR spectrum of the ZIF-67/$LaFeO_3$ nanocomposite exhibited characteristic vibrational bands of both ZIF-67 and $LaFeO_3$, confirming the successful coupling of ZIF-67 with $LaFeO_3$ in the composite material.

3.2 Ultraviolet-Visible Diffuse Reflectance Spectroscopy (UV-DRS) analysis

UV-Vis diffuse reflectance spectroscopy was used to assess the optical characteristics of the synthetic sample.[41] The optical characteristics of the collected photocatalysts were evaluated in the UV-visible wavelength range of 200–800 nm using UV-DRS (Fig. 3). In comparison to pure $LaFeO_3$ and ZIF-67 photocatalysts, the absorption margins of the ZIF-67/$LaFeO_3$ nanocomposite moved to a wider wavelength range, as shown in Fig. 3a. The co-ordination environment of Co(II) ions with 2-methylimidazole produced three discernible absorption peaks at 537, 565, and 590 nm in ZIF-67, which are suggestive of spin-coupled $^4A_2(F) \rightarrow {}^4T_1(P)$ transitions in tetrahedral Co(II).[42] The electronic transition from the V.B. (valence band) to the C.B. (conduction band) ($O_{2p} \rightarrow Fe_{3d}$) is responsible for the absorption edge of the $LaFeO_3$ sample, which is greater than 550 nm.[43] This finding suggests that the $LaFeO_3$ sample may function as a photocatalyst powered by visible light. Notably, with the addition of $LaFeO_3$, the ZIF-67/$LaFeO_3$ composite demonstrated much higher visible light absorption intensity in the 400–700 nm range. The bandgap energy of the ZIF-67, $LaFeO_3$ and

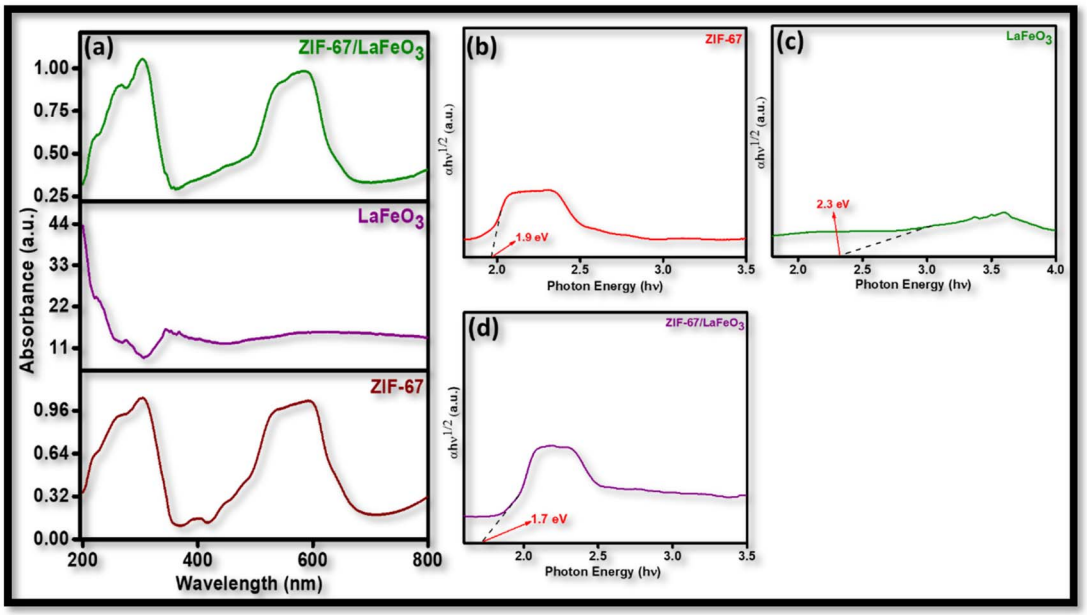

Fig. 3 The UV-vis (a) absorption spectra; Tauc plots for (b) ZIF-67, (c) $LaFeO_3$ and (d) ZIF-67/$LaFeO_3$.

ZIF-67/$LaFeO_3$ photocatalysts was computed from Tauc plots using the Kubelka–Munk formula:[34]

$$\alpha(h\upsilon) = \left(h\upsilon - E_g\right)^{\frac{1}{n}} \quad (17)$$

where α, $h\upsilon$, and E_g are the optical absorption, incident photon energy, and bandgap energy, respectively. The value of n is dependent on the kind of material; for direct and indirect semiconductors, it is equal to 0.5 and 2, respectively. Using eqn (18), the amount of $h\upsilon$ can be determined.[44]

$$h\upsilon = \frac{1240}{\lambda} \quad (18)$$

Bandgaps for pure ZIF-67, $LaFeO_3$, and ZIF-67/$LaFeO_3$ nanocomposites are determined using eqn (18) to be 1.9, 2.3, and 1.7 eV, respectively. The findings shown in Fig. 3b–d verify that $LaFeO_3$ lowers the ZIF-67 band gap energy from 1.9 to 1.7 eV.

3.3 Field emission scanning electron microscopy (FE-SEM) analysis

The morphologies and structures of ZIF-67, $LaFeO_3$ and ZIF-67/$LaFeO_3$ were examined using FE-SEM, as shown in Fig. 4. The smooth-surfaced ZIF-67 nanoparticles, which have an average size of 500 nm, exhibit a consistent rhombic dodecahedra structure as a result of the coordination bonds between Co ions and 2-methylimidazole, Fig. 4a–c display the EDS spectra and elemental mapping of ZIF-67 with C, N, O, and Co as the constituent elements, respectively. The FE-SEM image of the as-prepared $LaFeO_3$ is shown in Fig. 4d, which shows a nanorod structure at around 500 nm. The EDS spectra and elemental mapping of $LaFeO_3$ with La, Fe, and O as the constituent elements are shown in Fig. 4e and f, respectively. The aggregated morphology and $LaFeO_3$ attachment on the surface of the rhombic dodecahedra of ZIF-67 are depicted in the FE-SEM image of ZIF-67/$LaFeO_3$, as shown in Fig. 4g. The overall structure of the composite was quite similar to that of the pure ZIF-67 framework. The uniform anchoring of $LaFeO_3$ onto the ZIF-67 surface creates intimate interfacial contact, which promotes effective charge separation and interfacial charge transfer across the heterojunction. This suggests that $LaFeO_3$ was either well-dispersed inside or encapsulated by the ZIF-67 framework.[45] The EDS spectra and elemental mapping of the ZIF-67/$LaFeO_3$ nanocomposite with La, Fe, Co, C, and O as the component elements are displayed in Fig. 4h and 2i, respectively.

In order to determine the average particle size for each sample, the particle size distribution histogram was fitted to the log-normal distribution function, which is expressed as:[46]

$$f(D) = \frac{1}{\sqrt{2\pi}\sigma_D}\exp - \frac{\ln^2\left(\frac{D}{D_0}\right)}{2\sigma^2} \quad (19)$$

where the standard deviation is denoted by σ_{sd} and the average particle size by D. As shown in Fig. 5, the log normal distribution function is typically fitted to the particle size distribution histogram for ZIF-67, $LaFeO_3$, and ZIF-67/$LaFeO_3$ samples. A typical fit between the log normal distribution function and the particle size distribution histogram for ZIF-67, $LaFeO_3$, and ZIF-67/$LaFeO_3$ is shown in Fig. 5a, b and c, respectively. The ZIF-67, $LaFeO_3$, and ZIF-67/$LaFeO_3$ particle sizes are calculated to be 18.31, 60.4, and 43.4 nm, respectively, with corresponding standard deviations of 1.27, 1.62, and 1.16 nm, respectively. This intermediate size indicates that ZIF-67 and $LaFeO_3$ work together to maintain a decent surface area while preventing excessive grain development. This optimized size plays a crucial

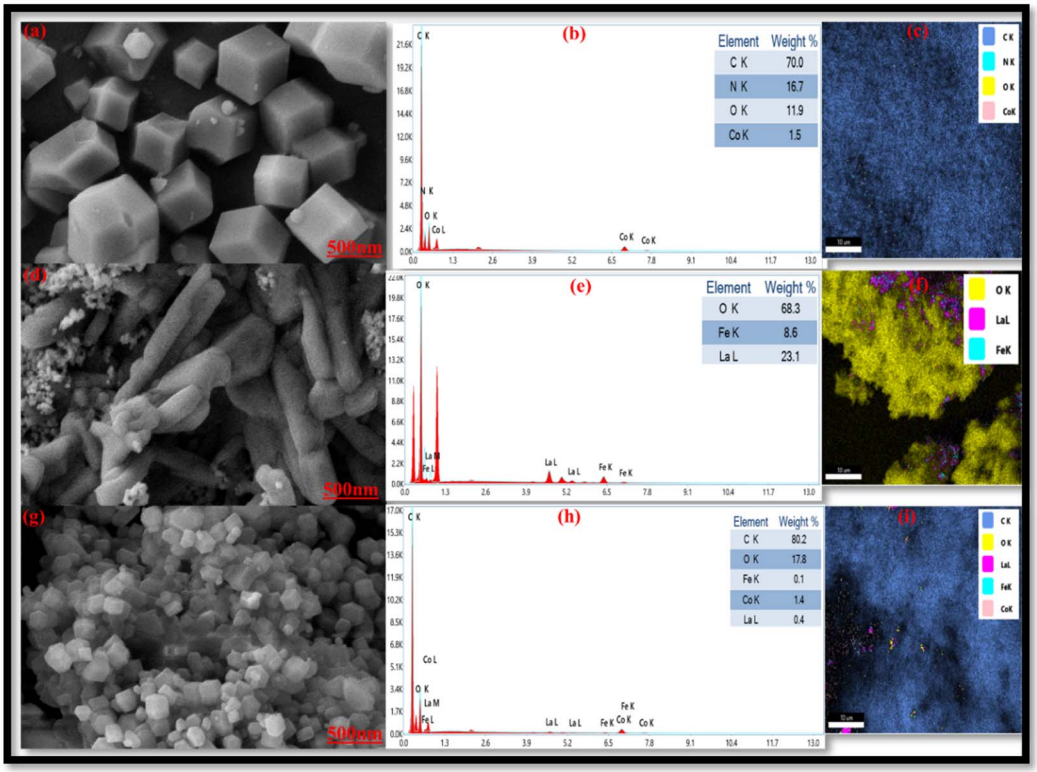

Fig. 4 FESEM micrograph of ZIF-67 (a), EDX spectrum of ZIF-67 (b), and elemental mapping of ZIF-67 (c); FESEM micrograph of $LaFeO_3$ (d), EDX spectrum of $LaFeO_3$ (e), and elemental mapping of $LaFeO_3$ (f); FESEM micrograph of ZIF-67/$LaFeO_3$ (g), EDX spectrum of ZIF-67/$LaFeO_3$ (h), and elemental mapping of ZIF-67/$LaFeO_3$ (i).

role in enhancing photocatalytic performance by providing a large effective surface area for reactant adsorption and light harvesting, while simultaneously limiting excessive grain growth that can hinder charge transport.[47] The reduced diffusion length in particles of moderate size facilitates faster migration of photogenerated charge carriers to the surface, thereby suppressing electron–hole recombination.

3.4 High Resolution Transmission Electron Microscopy (HR-TEM) analysis

HR-TEM, which provides high resolution lattice level information to supplement the FE-SEM analysis, was used to further investigate the microstructural details and crystallinity of the synthesized materials. It was used to evaluate the ZIF-67/$LaFeO_3$ composite in order to better investigate its tiny multiphase structure, as shown in Fig. 6a and b. The crystallinity of the composite observed in Fig. 6c was described using the SAED pattern. The polycrystalline nature of the composite is confirmed by the SAED ring pattern. The orthorhombic structure of the ZIF-67/$LaFeO_3$ composite may be used to index the diffraction rings. In the SAED pattern, weak diffraction rings or spots attributed to ZIF-67 can also be seen. For instance, the SAED pattern indicates the ZIF-67 and ZIF-67/$LaFeO_3$ (002) diffraction rings. The SAED finding suggests that ZIF-67, when

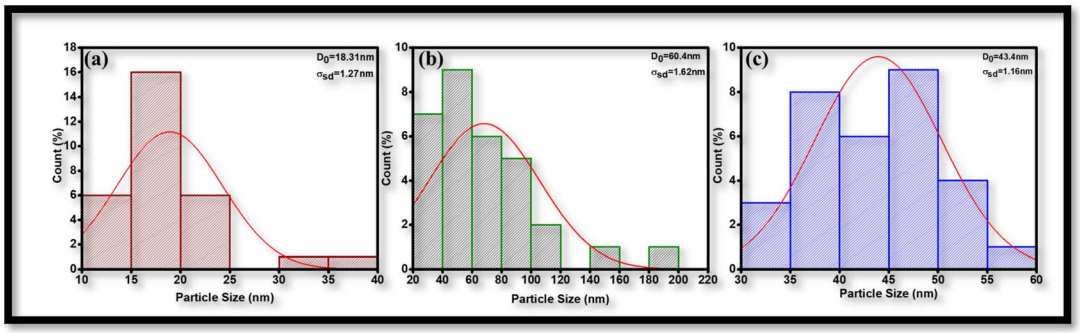

Fig. 5 Crystal size distribution graphs of (a) ZIF-67, (b) $LaFeO_3$, and (c) ZIF-67/$LaFeO_3$, respectively.

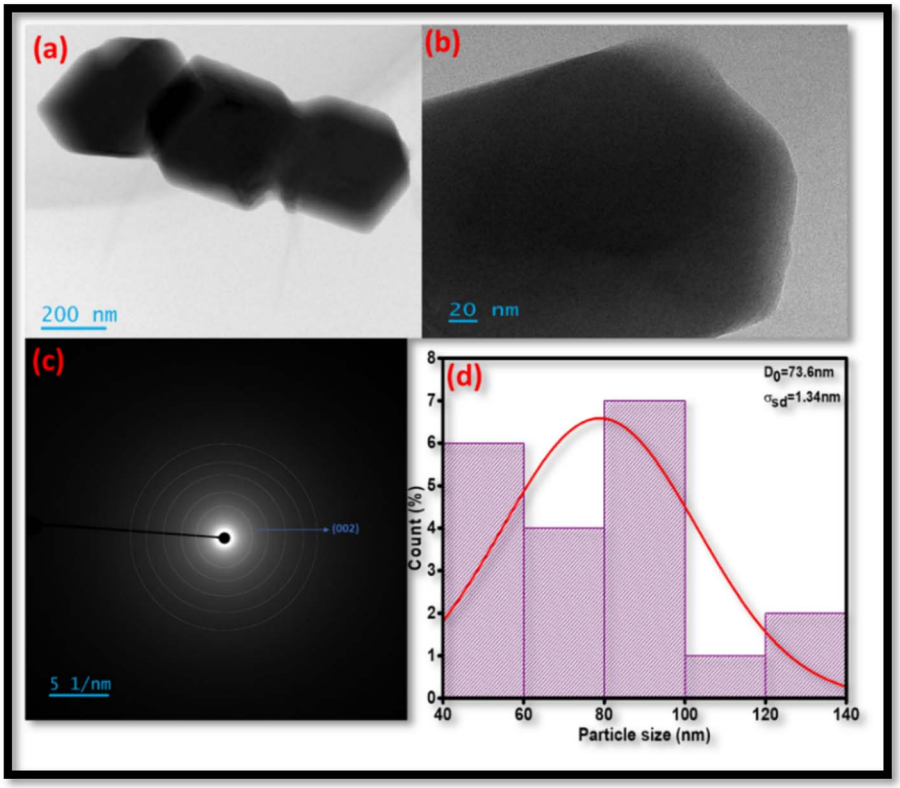

Fig. 6 TEM micrographs at 200 nm (a) and 20 nm (b), SAED pattern (c), and particle size distribution of the ZIF-67/$LaFeO_3$ nanocomposite (d).

evenly distributed inside or encapsulated with $LaFeO_3$, does not suffer structural change and instead stays in the rhombic dodecahedral phase. The computed particle size of the ZIF-67/$LaFeO_3$ composite is 73.6 nm, with a 1.34 nm standard deviation (Fig. 6d). The structural homogeneity and nanoscale characteristics are confirmed by HR-TEM. In addition to HR-TEM analysis, which verified the close lattice contact between the two phases, BET surface area analysis further supported the morphological observations from FE-SEM, which showed the polyhedral structure of ZIF-67 and the uniform distribution of $LaFeO_3$ nanoparticles. In order to validate the porous framework proposed by microscopic analyses, BET offered quantitative insights into the textural characteristics of the composite, such as specific surface area and pore size distribution.

3.5 Brunauer–Emmett–Teller (BET) analysis

Nitrogen adsorption–desorption analysis was carried out to assess the textural characteristics of the produced ZIF-67, $LaFeO_3$, and ZIF-67/$LaFeO_3$ nanocomposite. The BET specific surface areas of ZIF-67, $LaFeO_3$, and ZIF-67/$LaFeO_3$ are determined to be 1181.4, 3.31482, and 1082.94 $m^2\ g^{-1}$, respectively, as shown in Fig. 7 and Table S1. The N_2 adsorption–desorption isotherm of ZIF-67 corresponds to a type-I isotherm (Langmuir type), which is characteristic of microporous materials. This is common for materials with micropores because of their large surface area, which limits pore-filling.[45] The type IV isotherm found in the BET study of $LaFeO_3$ indicates the existence of mesoporous structures, which is favourable for photocatalytic applications due to enhanced mass transport and accessibility of active sites.[48] The type I isotherm of the ZIF-67/$LaFeO_3$ composite indicates that the composite maintains a microporous structure similar to that of ZIF-67 despite the incorporation of $LaFeO_3$. This observation indicates that ZIF-67 predominantly governs the surface area and pore structure of the composite, while $LaFeO_3$ primarily contributes to improved catalytic functionality rather than increasing overall porosity. In

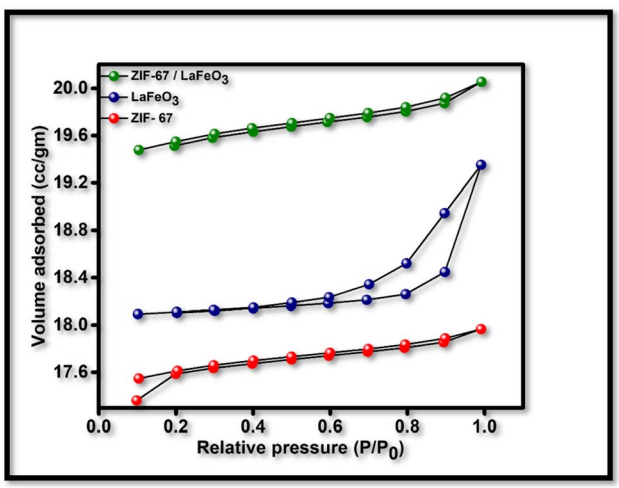

Fig. 7 N_2 adsorption/desorption isotherms of ZIF-67, $LaFeO_3$, and ZIF-67/$LaFeO_3$.

comparison to ZIF-67, the as-synthesized ZIF-67/$LaFeO_3$ exhibits a lower specific surface area, which might be caused by the heavier and nanoporous $LaFeO_3$ cores. However, compared to $LaFeO_3$, the BET surface area of ZIF-67/$LaFeO_3$ increases.[49,50] The BET study indicates that ZIF-67, $LaFeO_3$, and ZIF-67/$LaFeO_3$ have pore sizes of 1.56, 4.31, and 1.82 nm, respectively,[51] indicating predominantly microporous characteristics for ZIF-67 and the composite, and mesoporosity for $LaFeO_3$. The total pore volumes of ZIF-67 (6.2903 $cm^3\ g^{-1}$), $LaFeO_3$ (1.6687 $cm^3\ g^{-1}$) and the ZIF-67/$LaFeO_3$ composite (6.0278 $cm^3\ g^{-1}$) show significant variation. In contrast to $LaFeO_3$, which showed significantly less porosity, ZIF-67 showed a significant pore volume, indicating its porous nature. Importantly, the large pore volume of ZIF-67 is largely preserved in the ZIF-67/$LaFeO_3$ composite, indicating that the incorporation of $LaFeO_3$ does not significantly disrupt the pore architecture. Overall, these results demonstrate that the ZIF-67/$LaFeO_3$ nanocomposite effectively combines the high surface area and porous structure of ZIF-67 with the catalytic activity of $LaFeO_3$. This synergistic combination makes the composite highly suitable for applications requiring both extensive surface exposure and enhanced functional performance, such as photocatalysis and environmental remediation.

3.6 X-ray photoelectron spectroscopy (XPS) analysis

XPS analysis was employed to elucidate the surface chemical composition and oxidation states of the constituent elements in the ZIF-67/$LaFeO_3$ composite. The distinctive signals of Co, La, Fe, O, C, and N are shown in the XPS survey spectrum, confirming the elemental composition at the surface of the ZIF-67/$LaFeO_3$ composite (Fig. 8a). As shown in Fig. 8b, the three peaks observed at 285.00 eV (C–C, C–H), 287.22 eV (C-OR), and 289.02 eV (O═C–O) are attributed to surface carbonaceous species, originating from adventitious carbon contamination on the ZIF-67/$LaFeO_3$ composite.[52] The highest location of Co^{2+} is represented by the division of the Co $2p_{3/2}$ and Co $2p_{1/2}$ binding energies at 781.43 eV and 797.04 eV. The other peak, which stands for Co^{3+}, has a higher binding energy for Co $2p_{3/2}$ and Co $2p_{1/2}$ at 785.1 eV and 801.2 eV, respectively (Fig. 8c). A single, distinct peak centred at around 399.0 eV can be seen in the XPS spectra of N 1s (Fig. 8d), which suggest that the nitrogen environment in the ZIF-67/$LaFeO_3$ composite is chemically homogeneous. The pyridinic nitrogen species linked to Co^{2+} centres *via* Co–N bonds in the imidazolate linker, a characteristic of ZIF-67 frameworks, is consistent with the dominating binding energy position. The absence of extra deconvoluted peaks indicates that nitrogen is mostly found in a single chemical state throughout composite formation, with minimal or no oxidation, protonation, or other chemical disturbances. In Fig. 8e, the O 1s XPS spectrum shows a single peak at 532.6 eV (H_2O).[53] The formal oxidation valence states of +2 and +4, respectively, are occupied by the La and Fe atoms. As seen in Fig. 8f, spin–orbit interaction causes the La 3d orbital to divide into two lines (La $3d_{5/2}$ and La $3d_{3/2}$), with each line being split into two by electron transfer from oxygen ligands to the La 4f orbital.[54] The final states with the configurations $3d^9 4f^0 L$ and $3d^9 4f^1 L$, where L indicates a hole on the oxygen ligands, are represented by the doublet structure of the La $3d_{5/2}$ and La $3d_{3/2}$ orbitals.[55,56] The presence of the La^{3+} oxidation state is confirmed by the binding energy locations of the La $3d_{5/2}$ ($4f^0$) and La $3d_{3/2}$ ($4f^1$) orbitals, which are determined to be 836.0 eV and 853.8 eV, respectively. The La 3d orbital splitting is around 16.8 eV, which is consistent with earlier research and typical of La^{3+} compounds.[57,58] The charge transfer mechanism between the O 2p orbital and the La 4f orbital is also responsible for the satellite peaks of La $3d_{5/2}$ and La $3d_{3/2}$, which are situated at 838.3 eV and 848.3 eV, respectively. According to Gunasekaran *et al.* and Masteralo *et al.*[57,59] The Fe 2p spectra of the composite (Fig. 8g) exhibit two main features: a broad high binding energy component centred at 730.5 eV and a distinct peak at 715.5 eV. These features, consistent with characteristic Fe signals, indicate the presence of Fe^{3+}. Notably, the Fe $2p_{3/2}$ peaks display slightly higher intensity than the $2p_{1/2}$ peaks, likely due to crystal field induced splitting.[60]

3.7 Cyclic Voltammetry (CV) analysis

The CV curves of the ZIF-67, $LaFeO_3$, and ZIF-67/$LaFeO_3$ electrodes at various scan rates (5–100 mV s^{-1}) are displayed in Fig. 9a, c and e. Using a 5 mM ferro/ferricyanide ($[Fe(CN)_6]^{3-}$/$[Fe(CN)_6]^{4-}$) redox pair in 1 M KCl as the electrolyte and a potential window spanning from −0.5 to 0.6 V *vs.* the reference electrode, the electrochemical performance was examined. Particularly for ZIF-67, the presence of faradaic pseudocapacitive behaviour is confirmed by the distinct redox peaks seen in the cyclic voltammetry curves. The surface redox transition of Co^{2+} to Co^{3+}, a distinctive electrochemical characteristic of cobalt-based MOFs, is linked to these peaks. During the anodic scan, hydroxide ions (OH^-) in the alkaline medium facilitate the oxidation of Co^{2+} to Co^{3+}, leading to the formation of surface bound cobalt oxyhydroxide species. The corresponding reduction peak during the cathodic scan confirms the electrochemical reversibility of this redox process. This reversible redox activity enhances electron transport at the electrode surface and contributes significantly to the overall, capacitive performance. The presence of such redox active sites supports the contribution of pseudo capacitance in addition to electric double layer capacitance, thereby increasing the energy storage capability of the electrode materials. Indeed, the pseudocapacitive contribution arising from these redox reactions plays a dominant role in determining the specific capacitance for ZIF-67, $LaFeO_3$, and ZIF-67/$LaFeO_3$.[61] As the scan rate increased, a proportional increase in peak current was observed for all electrodes, indicating that the electrochemical processes are predominantly surface-controlled. This behaviour is characteristic of pseudocapacitive systems and is supported by the linear relationship between peak current and scan rate. Furthermore, the CV curves retained a nearly symmetrical shape and consistent profile across a wide range scan rates, demonstrating excellent electrochemical reversibility. The minimal variation in anodic and cathodic peak currents with increasing scan rate further confirms the highly reversible redox processes occurring at the electrode–electrolyte interface.

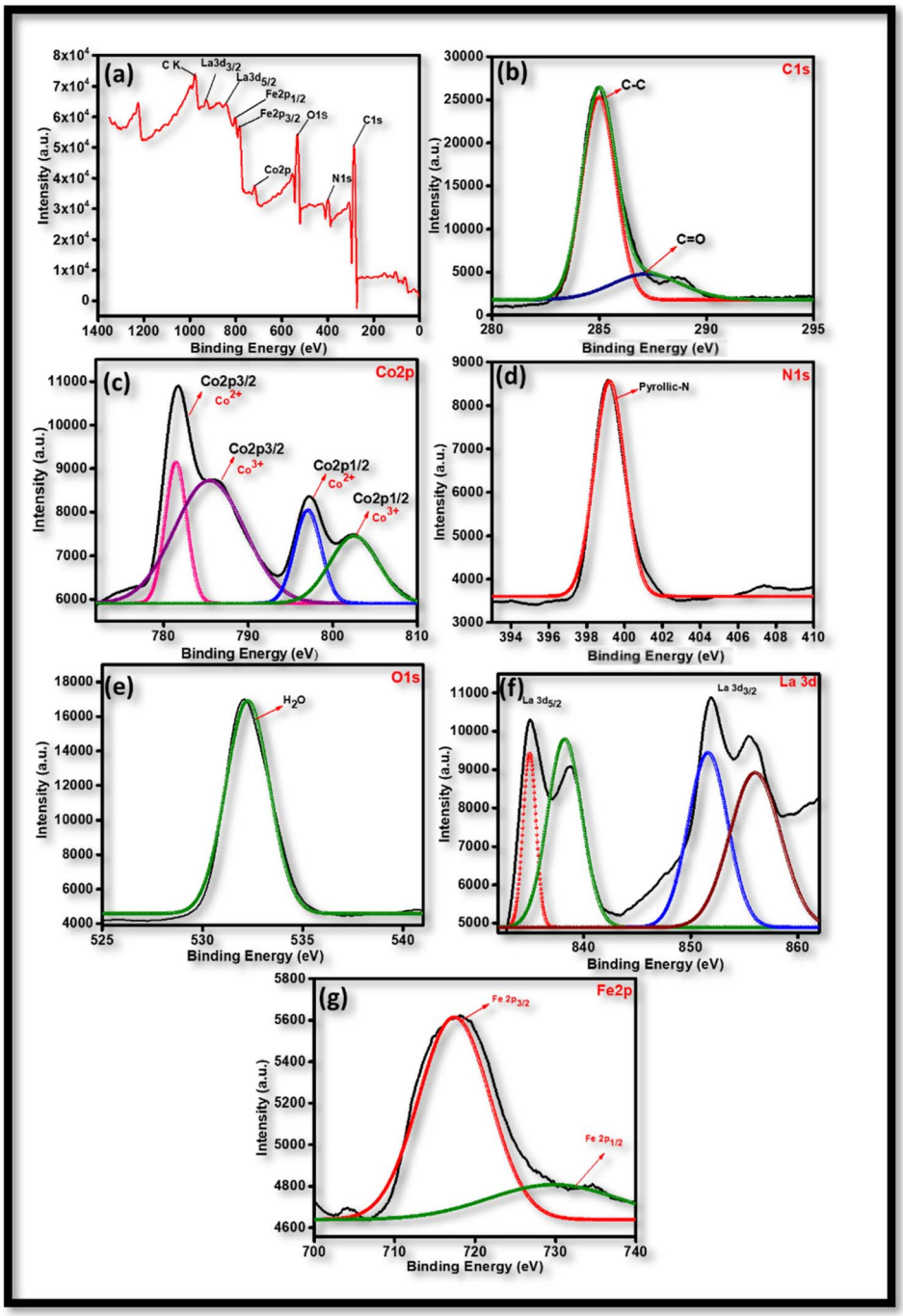

Fig. 8 (a) Wide survey X-ray photoelectron spectrum of as-prepared ZIF-67/$LaFeO_3$ and core level spectra of (b) C 1s, (c) Co 2p, (d) N 1s, (e) O 1s, (f) La 3d, and (g) Fe 2p.

In particular, the ZIF-67/$LaFeO_3$ composite, which gains from the synergistic interactions between the MOF and perovskite phases, is shown to have strong and sustained redox activity. The variation in the anodic peak positions toward more positive and cathodic peak positions toward more negative potentials are explained by the quasi-reversible character of the Co^{2+}/Co^{3+} redox pair. The kinetic behaviour of the redox process is reflected in these changes. The higher electrochemical performance of the composite electrode is a result of its increased electrical conductivity and large number of accessible active sites, which further promote effective charge transfer and improve electron transfer and ion diffusion trough the composite electrode. These factors were the reasons for the increase in current in ZIF-67/$LaFeO_3$ as compared to ZIF-67 and $LaFeO_3$. It should be noted that the redox reaction [Co(II)/Co(III) couple] in ZIF-67/$LaFeO_3$ occurs at lower potentials than in ZIF-67 and $LaFeO_3$, as seen from the voltammograms. This further demonstrates the better electrical conductivity of the ZIF-67/

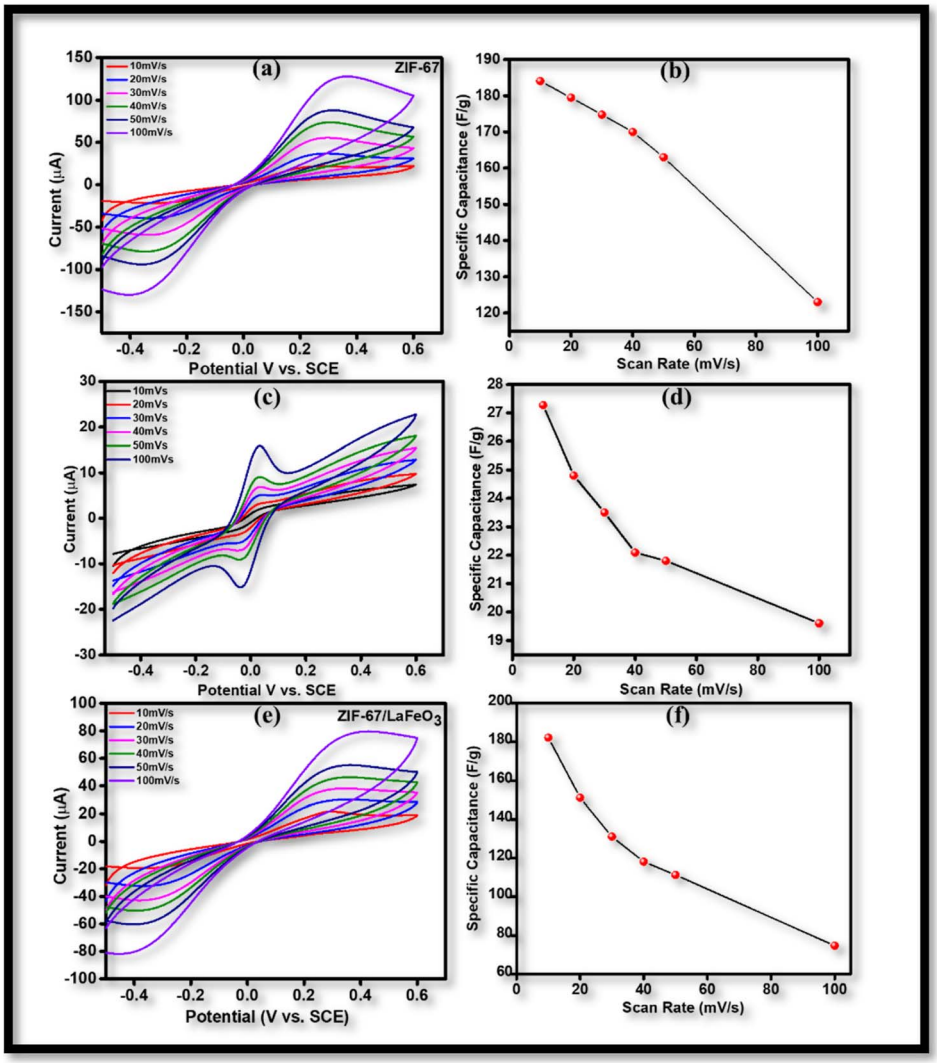

Fig. 9 The scan rate dependence of cyclic voltammetry curves for (a) ZIF-67, (c) $LaFeO_3$, and (e) ZIF-67/$LaFeO_3$ nanocomposite (10–100 mV s^{-1}), and the scan rate dependence of specific capacitance for (b) ZIF-67, (d) $LaFeO_3$ and (f) ZIF-67/$LaFeO_3$ nanocomposite across a scan rate range of 10–100 mV s^{-1}.

$LaFeO_3$ composite electrode. Fig. 9b, d and f illustrate how the specific capacitance changes in relation to the scan rate. With an increase in scan rate, it is clear that the specific capacitance falls. The outer surface and interlayer areas are the primary sites of interaction for electrolyte ions at higher scan rates because they do not have enough time to completely permeate the bulk of the electrode material. Consequently, the overall specific capacitance decreases since a sizable amount of the electrode is left unused. In order to determine the specific capacitance value and the voltammetric peak separation for ZIF-67, $LaFeO_3$, and ZIF-67/$LaFeO_3$ coated electrodes within the potential range of −0.5 V to 0.6 V, CV data were then recorded at various scan rates. The electron rate transfer constant was calculated using the Nicholson equation:

$$\psi = \frac{(-0.6288 + 0.0021X)}{1 - 0.017X} \quad (20)$$

Here,

$$X = E_{pa} - E_{pc} \quad (21)$$

$$\psi = k_s(\pi D n v F/RT)^{-1/2} \quad (22)$$

where ψ is the dimensionless kinetic parameter, E_{pa} and E_{pc} are the anodic and cathodic peak potentials, K_s is the heterogeneous electron transfer rate constant, D is the diffusion coefficient, v is the scan rate, F is the Faraday constant (96 485 C mol^{-1}), R is the universal gas constant (8.314 J mol^{-1} K^{-1}) and T is the absolute temperature. Among the tested materials, ZIF-67 exhibited the highest capacitance (123.8 F g^{-1}), followed by the ZIF-67/$LaFeO_3$ nanocomposite (74.3 F g^{-1}) and $LaFeO_3$ (19.6 F g^{-1}), as summarized in Table S2. Although ZIF-67/$LaFeO_3$ displays a lower specific capacitance, its synergistic charge separation, enhanced absorption of visible light, increased active sites and redox centres, and improved electron transfer kinetics make it particularly promising for photocatalysis and sensing. These findings are further supported by the frequency

dependent real and imaginary impedance behaviour (SI Fig. S1), which confirms effective charge transfer over a broad frequency range.

3.8 Electrochemical impedance spectroscopy (EIS) analysis

The EIS Nyquist plots of ZIF-67, $LaFeO_3$, and the ZIF-67/$LaFeO_3$ composite are shown in Fig. 10a. These measurements were performed to evaluate the interfacial charge transfer characteristics of the materials. In the Nyquist plots, the semicircle arc observed in the high frequency domain corresponds to the charge transfer resistance (R_{ct}), whereas the inclined linear portion in the low-frequency region is associated with Warburg impedance, which reflects ion diffusion processes within the electrode material and electrolyte. As shown in Fig. 10b, $LaFeO_3$ exhibits a pronounced semicircle followed by a discernible linear tail, indicating considerable resistance to charge transfer as well as some diffusion behaviour. The R_{ct} is directly related to the ease of electron transport within the catalyst matrix.[62] Notably, the formation of the ZIF-67/$LaFeO_3$ nanocomposite results in a significant reduction in R_{ct}, demonstrating enhanced interfacial charge transfer compared to pristine $LaFeO_3$ and ZIF-67. This improvement highlights the beneficial role of composite formation in facilitating electron transport across the electrode–electrolyte interface.

The fitted equivalent circuit parameters of ZIF-67, $LaFeO_3$, and ZIF-67/$LaFeO_3$ at room temperature are summarized in Table S3. The experimental impedance data (Z' and Z'' as a function of frequency) were analysed using ZSIMPWIN-2 software by fitting them to an equivalent circuit model represented as $LRQ(CR)$. The electrical parameter that corresponded to the potential electric circuit could be obtained. For instance, in the $LRQ(CR)$ current circuit, "L", "C", "Q", and "R" stand for L: inductance, C_b: bulk capacitance, Q: constant phase element, and R_b: bulk resistance. The acquired C_b, Q, and R_b, together with R_{gb}: grain-boundary resistance and C_{gb}: grain-boundary capacitance, may be obtained when the fitted circuit is $LRQ(CR)$. The extracted electrical parameters reveal distinct trends among the materials. In particular, it states that the ZIF-67/$LaFeO_3$ composite has the maximum inductance, which can promote improved charge separation and less recombination, hence increasing photocatalytic efficacy. In addition, ZIF-67 and the ZIF-67/$LaFeO_3$ composite have the lowest bulk resistance compared to $LaFeO_3$, which enhances electrical conductivity. The impedance spectra were analysed using the $LRQ(CR)$ equivalent circuit model in order to extract important electrical characteristics, including capacitance, characteristic power frequency, grain resistance (R_g), and grain boundary resistance (R_{gb}). This modelling technique successfully distinguishes the distinct contributions to the total electrical response from the bulk material (grain interiors), grain borders, and electrode–electrolyte interfaces. The fitted Nyquist plots exhibit distinct semicircular arcs and linear regions, corresponding to different resistive and capacitive elements within the system. Grain boundary resistance documents the obstacle to charge flow at intergranular junctions, whereas grain resistance represents charge transport inside the crystalline domains. Polarization effects are also evident in the low-frequency tail, which is influenced by the electrode contact. When taken as a whole, the impedance analysis provides a through comprehension of the charge transport dynamics and identifies the key factors governing the electrical behaviour of the materials under investigation. The extracted parameters indicate that $LaFeO_3$ exhibits relatively high grain-boundary capacitance, while ZIF-67 shows comparatively lower grain-boundary resistance. In contrast, the ZIF-67/$LaFeO_3$ nanocomposite displays intermediate values of both grain-boundary resistance and grain-boundary capacitance, positioned between those of ZIF-67 and $LaFeO_3$. This suggests that the composite material achieves an optimal balance between efficient charge transport and sufficient resistance, contributing to its enhanced electrochemical and photocatalytic performance.

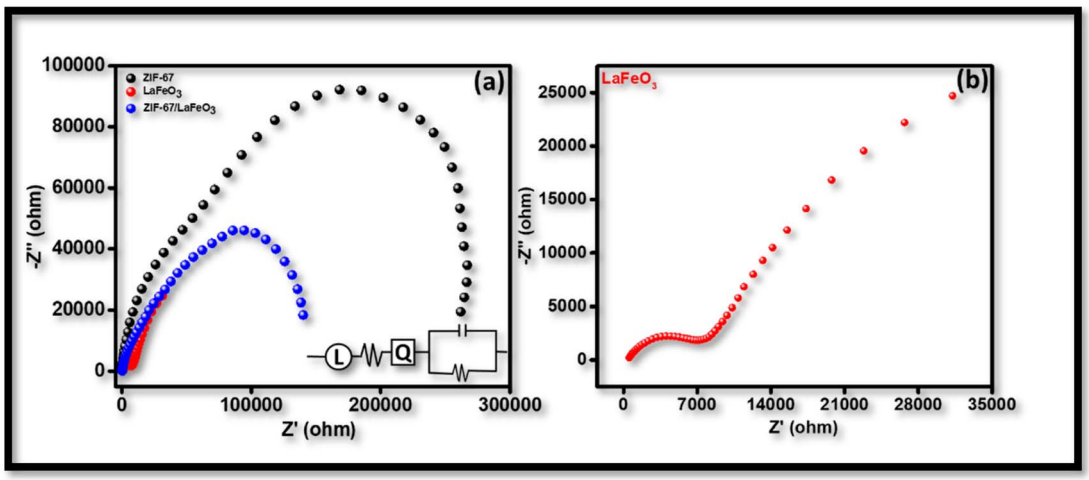

Fig. 10 (a) Nyquist plots obtained from electrochemical impedance spectroscopy (EIS). (a) Comparative Nyquist plots of ZIF-67, $LaFeO_3$, and the ZIF-67/$LaFeO_3$ nanocomposite, along with the corresponding equivalent electrical circuit used for fitting. (b) Enlarged Nyquist plot of pristine $LaFeO_3$ highlighting its charge-transfer behaviour.

3.9 Mott–Schottky study

To examine the band structures of ZIF-67 and $LaFeO_3$ in more details, the M–S plot was extrapolated using the following formula to get the flat-band potential of ZIF-67 and $LaFeO_3$. The findings are shown in Fig. 11a and b.

$$\frac{1}{C^2} = \frac{2}{N_D e \varepsilon_0 \varepsilon} = \left(E - E_{fb} - \frac{kT}{e}\right) \quad (23)$$

where E is the bias voltage, E_{fb} is the fat band potential, T is the temperature, k is the Boltzmann constant, C is the capacitance of the semiconductor space charge layer, N_D is the carrier density of the electron, e is the basic charge value, ε_0 is the dielectric constant of the vacuum, and ε is the relative dielectric constant of the semiconductor. The findings show that ZIF-67 is an n-type semiconductor, since the linear graphs have a negative slope. The Fermi level is represented by the flat band potential. For ZIF-67, the flat-band potential (E_{fb}) is −0.34 V *vs.* SCE.[63] The E_{CB} of an n-type semiconductor is often more negative than the E_{fb} by −0.1 or −0.2 V, but the E_{VB} of a p-type semiconductor is higher by 0.1 or 0.2 V. The synthetic $LaFeO_3$ is a p-type semiconductor, as shown by the negative slope in the linear section of the plot. The Mott–Schottky (M–S) plot, in which the *x*-axis intercept is around 1.4 V *versus* the normal hydrogen electrode (NHE), was used to calculate the flat-band potential of $LaFeO_3$. Because of the location of the Fermi level in relation to the VB, the flat-band potential for p-type semiconductors is usually found to be around 0.1 V below the valence and boundary. In regard to this, it is possible to estimate that the valence band potential of $LaFeO_3$, which accounts for the conversion between reference electrodes, is around 1.5 V (*vs.* NHE) or 1.9 V *vs.* the saturated calomel electrode (SCE). For $LaFeO_3$, a well-known p-type perovskite oxide, our estimate agrees with values given in the literature. Establishing the VB position is essential for building the energy band diagram and comprehending the band alignment of ZIF-67/$LaFeO_3$, which controls the dynamics of charge transfer and photocatalytic activity.[64] This formula may be used to get the standard band potential (*vs.* NHE):

$$E\ (vs.\ \text{NHE}) = E(vs.\ \text{SCE}) + 0.244\ \text{V} \quad (24)$$

The valence band (VB) location of $LaFeO_3$ is therefore calculated to be around 2.14 V in relation to the normal hydrogen electrode (NHE). The conduction band (CB) location is estimated to be around 0.004 V *vs.* NHE based on the findings of UV-vis absorption spectroscopy and electrochemical experiments. There is consistency between the optimal and theoretical methods, as this experimentally determined value closely matches the conduction band edge of −0.1 V estimated using Mulliken electronegativity theory (Table S4). The precise band alignment of $LaFeO_3$ is further supported by our results, which is essential for comprehending its function in the ZIF-67/$LaFeO_3$ heterojunction as well as its contribution to efficient charge separation and photocatalytic performance.

4. Electrochemical sensing behaviour of CFX at the ZIF-67/$LaFeO_3$/SPCE

The electrochemical behaviour of bare and modified electrodes was initially examined using CV in 0.1 M KCl containing 5 mM $[Fe(CN)_6]^{3-/4-}$ to evaluate interfacial charge-transfer characteristics. Subsequently, the ZIF-67/$LaFeO_3$ nanocomposite-modified SPCE was used to investigate the voltammetric response of CFX. Owing to the pharmacological relevance of CFX and the need for sensitive detection, a systematic electrochemical study was performed to elucidate the sensing behaviour, governing mechanism, and kinetics of electron transfer at the hybrid electrode interface.

4.1 The effect of pH

The pH of the supporting electrolyte plays a critical role in controlling the electrochemical response of CFX by influencing its protonation state and redox activity at the electrode–electrolyte interface. Therefore, optimization of pH is essential to achieve maximum sensitivity and reproducibility. As shown in Fig. 12a, CV measurements of 100 ppm CFX were performed in

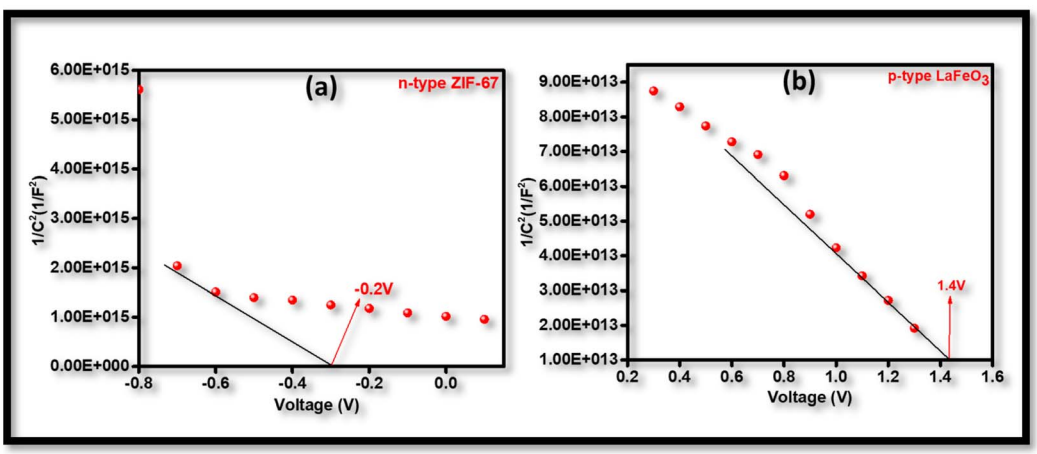

Fig. 11 Mott–Schottky plots of (a) n-type ZIF-67 and (b) p-type $LaFeO_3$.

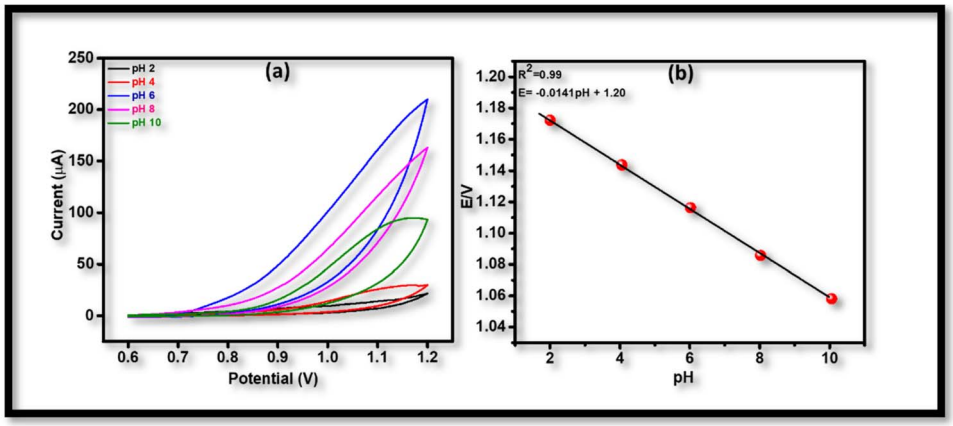

Fig. 12 (a) Detection of CFX on the ZIF-67/$LaFeO_3$ composite at different pH values, and (b) calibration curve of the pH graph.

40 mM Britton–Robinson (BR) buffer over a pH range of 2–10 (2,4,6,8 and 10) and a scan rate of 100 mV s^{-1}. CFX oxidation potentials showed a clear trend, shifting toward less positive values as the pH increased above 2, indicating that the oxidation process was facilitated under less acidic conditions. The highest oxidation current was obtained at pH 6, suggesting that CFX undergoes the most efficient electrochemical oxidation at near-neutral pH. In strongly acidic media (pH 2 and 4), excess protonation of electroactive functional groups suppresses oxidation or alters the reaction pathway, leading to a reduced current response. Conversely, under highly basic conditions (pH 10), extensive deprotonation diminishes electrochemical activity, resulting in lower sensitivity. Thus, pH 6 was identified as the optimal condition for CFX electrooxidation at the ZIF-67/$LaFeO_3$/SPCE surface.

A pH dependent change in the redox behaviour of CFX is shown in Fig. 12b, which shows a linear connection between the oxidation potential (E_p) and pH, expressed by the relation:

$$E_p/V = -0.0141\ pH + 1.20\ (R^2 = 0.99) \quad (25)$$

This excellent linearity demonstrates the electrochemical stability of the ZIF-67/$LaFeO_3$ composite and indicates effective proton-coupled electron transfer (PCET) at the electrode interface. Since it shows the involvement of protons in the rate limiting stages and the ideal circumstances for catalytic degradation, the pH dependence of the redox potential is important in the context of CFX degradation. However, the observed slope ($\sim$−14 mV pH^{-1}) is significantly lower than the theoretical Nernstian value of −59 mV pH^{-1} expected for a one-electron/one-proton process. This deviation suggests a more complex, multi-step redox mechanism, where electron transfer may precede proton involvement or where protons participate in a secondary equilibrium step. A more sophisticated process, such as protonation after electron transfer or proton involvement in a secondary equilibrium, may be indicated by the narrower slope, which suggests partial proton dependency. These findings imply that the electrochemical signal of CFX is constant in various media, with no discernible variation found in 40 mM BR buffer at pH 6 in contrast to other investigated circumstances. Based on these results, 40 mM BR buffer at pH 6 was selected as the optimal medium for all subsequent measurements. Scheme S1 shows the synthesis procedure for the formation of the ZIF-67/$LaFeO_3$ electrode for electrochemical sensing.

4.2 The effect of concentration

The concentration-dependent electrochemical response of CFX was investigated using CV at the ZIF-67/$LaFeO_3$-modified SPCE under optimized conditions (40 mM BR buffer, pH 6). As shown in Fig. 13a, a well-defined anodic peak corresponding to CFX oxidation was observed, with the peak current increasing progressively as the concentration increased from 5 to 40 ppm. This behaviour confirms the effective electrocatalytic activity of the modified electrode toward CFX oxidation. The steady increase in the peak current shows efficient electron transfer and stable electrode–analyte interaction. The maximum oxidation current was observed at 40 ppm, corresponding to optimal utilization of active catalytic sites. A virtually identical current was seen at 10 ppm, producing a strong reaction. A significant decline in current occurs beyond 40 ppm, likely due to surface saturation or partial blockage of active sites by excess analyte. This behaviour suggests that the sensing process involves an initial adsorption-controlled regime at low-to-moderate concentrations, followed by site saturation at higher concentrations.

The calibration curve (Fig. 13b) exhibited a linear response over the concentration range of 5–100 ppm, described by the equation:

$$I = -6.154X + 632.5\ (R^2 = 0.99) \quad (26)$$

The conventional formula (LOD = $3s/m$) was used to assess the limit of detection (LOD), where s is the standard deviation of blank signal (or low-concentration sample response) and m is the slope of the linear calibration curve, which indicates the sensitivity of the procedure. The first linear equation yielded a LOD of 3.41 ppm. It should be noted that the LOD, which was

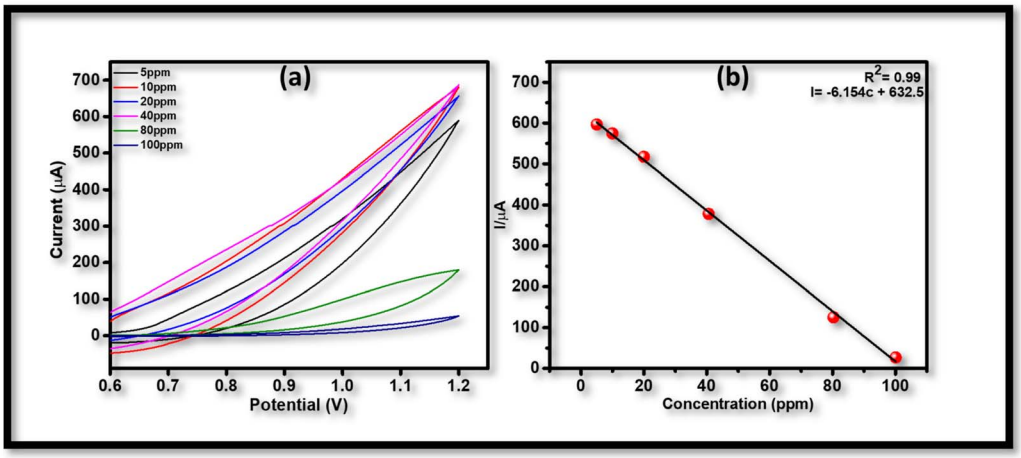

Fig. 13 (a) Detection of CFX on the ZIF-67/$LaFeO_3$ composite at different concentrations, and (b) calibration curve of the concentration graph.

calculated using the slope technique and the response, is subject to the impact of detection sensitivity and experimental accuracy, which may occasionally result in the LOD exceeding the maximum concentration range. Similar to the LOD, the slope method and the standard deviation of the responses may be used to determine the limit of quantification (LOQ = $10s/m$),[65] yielding a LOQ of around 10.33 ppm. The overall exceptional performance of the ZIF-67/$LaFeO_3$/SPCE demonstrates its promise as a dependable platform for the electrochemical measurement of CFX in actual samples. A comparative study of the sensing of CFX using different modified electrodes is given in Table S6.

4.3 Mechanistic understanding of sensing of CFX using ZIF-67/$LaFeO_3$

The electrochemical sensing of CFX at the ZIF-67/$LaFeO_3$-modified SPCE is governed by a synergistic combination of molecular adsorption, surface-assisted oxidation, and redox-mediated electron transfer. Similar mechanistic frameworks have been established for nanostructured electrodes, such as carbon nanofiber-based systems, where enhanced sensitivity is attributed to adsorption-controlled processes and accelerated interfacial charge transfer rather than purely diffusion-limited transport. Primarily, the abundant surface functionalities and hierarchical porosity of the ZIF-67/$LaFeO_3$ nanocomposite facilitate strong adsorption of CFX molecules through hydrogen bonding and coordination interactions involving surface hydroxyl groups, metal centres, aminothiazole substituents, and β-lactam carbonyl. The anchoring of CFX is further improved by the presence of oxygen vacancies in $LaFeO_3$, which makes it easier for it to preconcentrate on the electrode surface. Upon application of anodic potential, the electrooxidation of CFX proceeds primarily through electron-rich functional groups, particularly the thioether side chain and β-lactam moiety, which produce reactive radical cation intermediates (Scheme 1). The oxidized fragments go through desulfurization and amide bond cleavage, which are electrochemically expressed as an anodic current response. The Co^{2+}/Co^{3+} and Fe^{3+}/Fe^{2+} couples found in the ZIF-67/$LaFeO_3$ framework mediate the electron transfer:

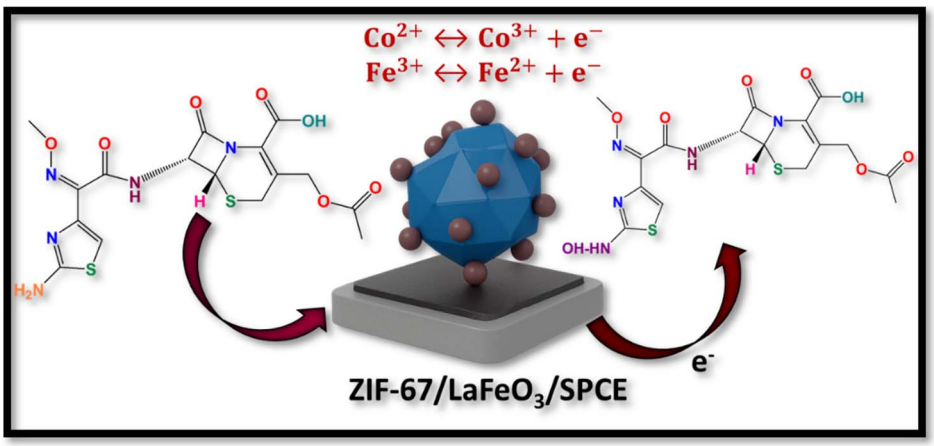

Scheme 1 Mechanism oxidation of CFX using the ZIF-67/$LaFeO_3$ nanocomposite.

$$CFX \rightarrow CFX^{\bullet+} + e^- \quad (27)$$

$$Co^{2+} \leftrightarrow Co^{3+} + e^- \quad (28)$$

$$Fe^{3+} \leftrightarrow Fe^{2+} + e^- \quad (29)$$

The Co^{2+}/Co^{3+} and Fe^{3+}/Fe^{2+} redox couples act as catalytic relays, lowering the activation barrier for CFX oxidation and accelerating heterogeneous electron transfer (HET). ZIF-67 provides a conductive framework that facilitates rapid charge shuttling, while $LaFeO_3$ contributes oxygen vacancies and strong electronic coupling, collectively enhancing charge separation and transport toward the SPCE current collector. This cooperative interaction results in a sharp, well-defined anodic peak whose magnitude scales linearly with CFX concentration within the dynamic range. The non-Nernstian pH dependence, concentration-dependent saturation behaviour, and enhanced voltammetric response collectively indicate that CFX sensing at the ZIF-67/$LaFeO_3$/SPCE is predominantly governed by a surface-confined, adsorption-assisted, proton-coupled electron transfer mechanism. Furthermore, selectivity arises from the specific electrochemical reactivity and surface affinity of CFX functional groups, whereas common interferents lacking such electroactive moieties exhibit negligible responses under identical conditions. The combination of ZIF-67 and $LaFeO_3$ results in increased sensitivity, decreased overpotential, and strong reproducibility, making the hybrid material an effective catalytic interface for CFX electroanalysis.

5. Photo-Fenton degradation of CFX

Iron-based compounds are known to be efficient Fenton catalysts, especially those having Fe(II) oxidation states.[66] In a photo-Fenton-like degradation of CFX in natural sunlight, the photocatalytic activities of the individual components (ZIF-67 and $LaFeO_3$) and their composite were compared. After 10 minutes of darkness to achieve adsorption–desorption equilibrium, the system was illuminated to guarantee accurate kinetic assessment. To evaluate the synergistic effects in the heterojunction system, degradation rates were tracked after exposure to visible light in the range of 200–500 nm, as shown in Fig. 14a. Therefore, 10 minutes was the ideal duration for optimizing the entire CFX photocatalytic process. A major factor in photocatalytic reactions is the adsorption of pollutants onto the surface of the catalysts.

The photocatalytic process was coupled with H_2O_2, and the degrading impact of the resulting composite system on CFX was also examined. As can be seen from Fig. 14b, only 4.2% of the CFX was degraded when there was only H_2O_2. At 75 minutes, the degradation efficiency of CFX under visible light irradiation was 74.1% and 67.3% when ZIF-67 and $LaFeO_3$ were employed, respectively, as a single photocatalyst without H_2O_2. Compared to $LaFeO_3$, ZIF-67 had a greater degradation efficiency for CFX, suggesting that it has a better photocatalytic activity. The ZIF-

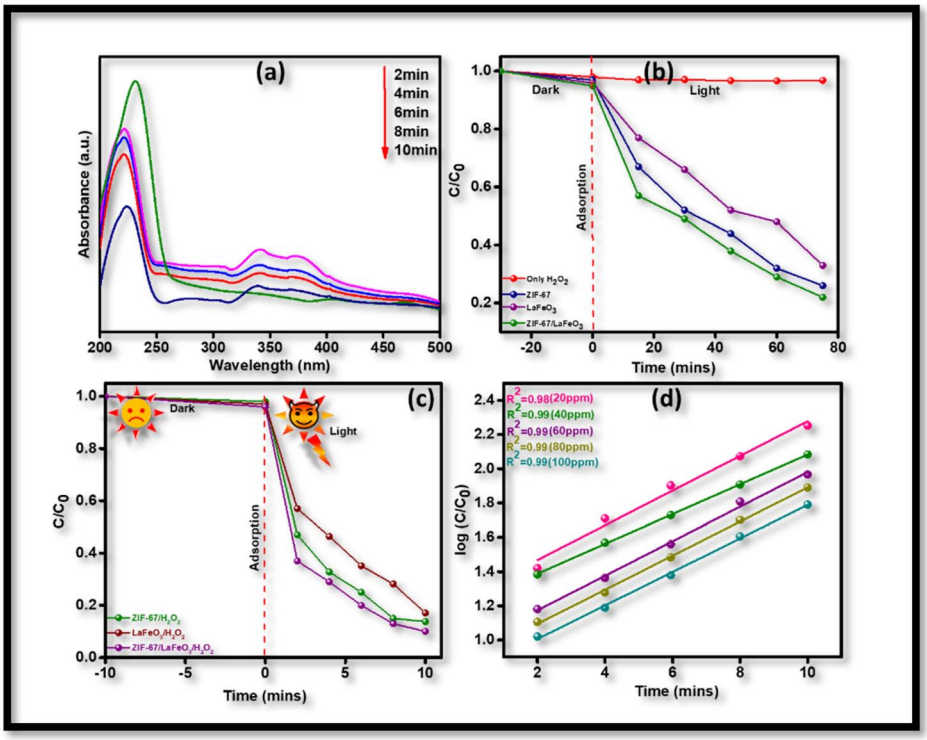

Fig. 14 Photocatalytic and photo-Fenton degradation behaviour of CFX over the ZIF-67/$LaFeO_3$ composite. Time-dependent UV-Vis absorption spectra of CFX during degradation (a); photocatalytic degradation profiles of CFX under visible-light irradiation in the absence of H_2O_2 (b); photo-Fenton degradation performance in the presence of H_2O_2 (c); and corresponding pseudo-first-order kinetic plots under different initial CFX concentrations (d).

67/$LaFeO_3$ composite showed significantly improved photocatalytic activity when compared to the separate variables, ZIF-67 and $LaFeO_3$. It is believed that this improvement is due to the close interfacial contact between ZIF-67 and $LaFeO_3$, which effectively separates photogenerated electron hole pairs and prevents their recombination. Due to the transfer of photogenerated carriers on the surface of the composite, the ZIF-67/$LaFeO_3$ composite was determined to be the most effective photocatalyst, removing 83.1% of the CFX in 75 minutes. The degrading process of CFX was greatly accelerated by the coupling of H_2O_2 and the photocatalyst when H_2O_2 was introduced, as shown in Fig. 14c. In 10 minutes, ZIF-67/H_2O_2 and $LaFeO_3$/H_2O_2 could reach greater degradation efficiencies of 80% and 75.1%, respectively, when 10 mM H_2O_2 is present. Additionally, the ZIF-67/$LaFeO_3$/H_2O_2 combination achieved 90.1% degrading efficiency of CFX in 10 minutes. According to the findings, CFX degradation is positively impacted by the addition of H_2O_2 during photocatalysis. Due to the fact that it serves as a source of hydroxyl radicals, which are in charge of the efficient breakdown of complex organic contaminants, it plays a vital and essential part in the photo-Fenton degradation of antibiotics. In the ZIF-67/$LaFeO_3$ nanocomposite, ZIF-67 acts as the matrix material by providing a porous and high surface area framework, while $LaFeO_3$ functions as the reinforcement component, supplying the photoactive semiconductor sites. The uniform dispersion of $LaFeO_3$ within the ZIF-67 matrix promotes interfacial charge transfer and enhances photocatalytic efficiency through synergistic effects.

The inclusion of H_2O_2 ensures ongoing radical formation by supporting the cyclic regeneration of iron ions (Fe^{2+}/Fe^{3+}) under light irradiation, in addition to increasing the degradation rate and mineralization efficiency.

Fig. 14d illustrates the enhanced photo-Fenton performance over a rage of drug concentrations. The following reaction kinetics of CFX degradation of the as-prepared materials were examined using pseudo-first-order kinetic dynamics.

$$\ln(C_0/C_t) = -kt \quad (30)$$

where C_0 represents the CFX concentration following adsorption equilibrium before irradiation, C represents the CFX concentration at irradiation time t, and k represents the apparent reaction rate constant. Furthermore, $t_{1/2}$ was calculated using the aforementioned equation. Generally speaking, $t_{1/2}$ is the time needed to break down CFX into half of its initial concentration and is shown in eqn (31).

$$t_{1/2} = 0.693/k_{app} \quad (31)$$

Table S5 provides a summary of the CFX degradation rate constant (k_{app}), correlation coefficient factor (R^2), and half-life value ($t_{1/2}$).

5.1. Effect of operational parameters

To gain a comprehensive understanding of the operational parameters governing photo-Fenton degradation over the ZIF-67/$LaFeO_3$ photocatalyst, the effects of several key factors, including catalyst loading, pH, oxidant volume, initial contaminant levels, and the presence of coexisting anions and cations, were systematically investigated. These studies provided critical insights into the reaction mechanism and enabled optimization of the operating conditions for enhanced photocatalytic efficiency.

The photocatalyst loading is a key factor in photocatalytic performance, and its optimization is essential for achieving both high efficiency and economic feasibility. As shown in Fig. 15a, the photo-Fenton degradation efficiency increased rapidly when the catalyst dosage was raised from 10 to 20 mg, owing to the increased availability of active sites and enhanced generation of reactive oxygen species ($OH^{\bullet}$, $O_2^{\bullet-}$, *etc.*). The optimal catalyst loading was determined to be 20 mg. However, further increasing the catalyst amount to 60 mg led to a decline in degradation efficiency, likely due to catalyst agglomeration, which reduces the accessible surface area and blocks active sites.

Additionally, the photocatalytic activity is negatively impacted by reduced photon absorption when the catalyst concentration exceeds its saturation point. This is explained by the overabundance of catalyst creating a barrier that hinders photon contact with active catalytic sites, limits the irradiation region, and blocks light penetration.[67]

The influence of solution pH on CFX degradation was examined due to its critical role in metal ion speciation and radical generation in Fenton-like systems. This analysis provided insight into pollutant degradation under different protonation states and helped identify optimal reaction conditions. As shown in Fig. 15b, degradation efficiencies of 60.2, 73.1, 81.3, and 65.7% were achieved for pH values of 2, 4, 6, and 8, respectively, clearly identifying pH 6 as the optimal reaction condition. On the other hand, abundant surrounding protons at a lower pH may trap $OH^{\bullet}$ radicals, preventing the conversion of Fe^{3+} ions and so reducing activity. Likewise, at a higher pH, the hydroxide ions that are generated form a barrier between Fe^{3+} and H_2O_2, which lowers the formation of $OH^{\bullet}$ and lowers activity. Furthermore, H_2O_2 dissociates to H_2O and O_2 molecules at higher pH values, which prevents the formation process altogether.[68] Importantly, zeta potential analysis shows that the composite surface exhibits a near neutral charge, which minimizes electrostatic repulsion between the catalyst surface and pollutant molecules, thereby facilitating effective adsorption and interfacial charge transfer (Fig. S3).

The effect of oxidant concentration (H_2O_2) on photo-Fenton degradation was investigated, as shown in Fig. 15c. Increasing the H_2O_2 dosage from 5 to 20 μL enhanced the CFX degradation efficiency from 67.8% to 91.2%, indicating that higher oxidant availability promotes $^{\bullet}OH$ radical generation and accelerates degradation kinetics. However, a further increase in H_2O_2 volume to 30 μL resulted in a reduced degradation rate, suggesting that excessive H_2O_2 acts as a radical scavenger and disrupts the balance between $^{\bullet}OH$ generation and consumption. Therefore, optimizing the H_2O_2 concentration is critical to achieving maximum photo-Fenton efficiency.[67] Additionally, as shown in Fig. 15d–f, the degradation kinetics of CFX under varying catalyst dosage, pH values, and H_2O_2 concentrations closely followed a pseudo-first-order kinetic model, suggesting

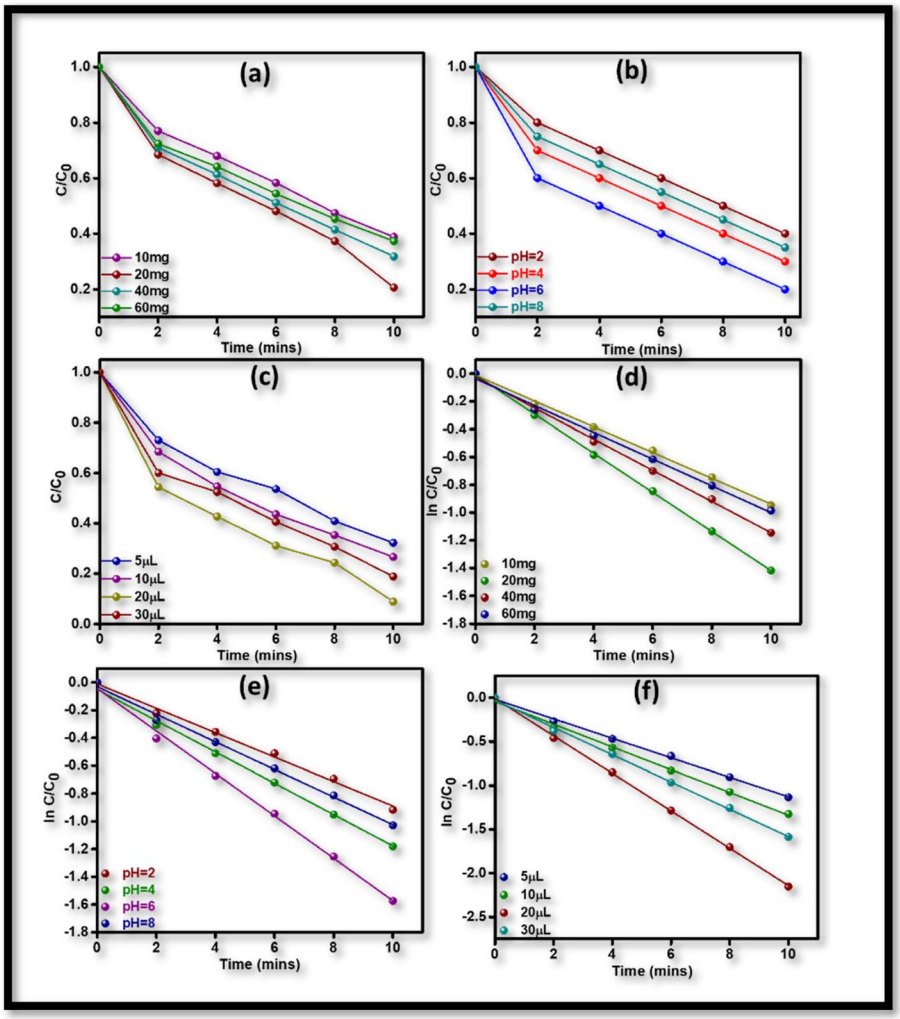

Fig. 15 The performance of the ZIF-67/$LaFeO_3$ photocatalyst is influenced by various operational parameters, including amount of photocatalyst (a), commencement pH (b), quantity of H_2O_2 (c), and the pseudo first-order kinetics associated with each parameter (d–f).

that the reaction rate was directly proportional to pollutant concentration. The observed trends in dose, oxidant level, and pH impact are supported by scavenging and reusability studies (SI Fig. S2), reinforcing the proposed degradation mechanism and the robustness of the ZIF-67/$LaFeO_3$ photocatalyst.

5.2 Possible photocatalytic mechanism

The development of a type-II p–n heterojunction in the ZIF-67/$LaFeO_3$ composite is responsible for the effective separation of electrons and holes. The valence and conduction band edges of ZIF-67 and $LaFeO_3$ were identified using Mulliken's electronegativity technique in order to clarify the semiconductor band alignment and heterojunction mechanism, as shown by eqn (32) and (33).[69]

$$E_{VB} = \chi - E^e + 0.5E_g \quad (32)$$

$$E_{CB} = E_{VB} - E_g \quad (33)$$

In this instance, χ stands for the absolute electronegativity, which is determined by taking the geometric mean of the electronegativities of the component constituents of semiconductors. ZIF-67 and $LaFeO_3$ have respective χ values of 5.02 (ref. 70) and 5.5 eV.[71] On the hydrogen scale, E^e stands for free electron energy (4.5 eV *vs.* NHE). Fig. 3a and b shows the E_g values of ZIF-67, $LaFeO_3$ and ZIF-67/$LaFeO_3$, which are 1.9, 2.3 and 1.7 eV, respectively.

The band locations of n-ZIF-67 and p-$LaFeO_3$ before and after contact are shown in Scheme 2a and b based on the aforementioned study. In the reaction system shown in Scheme 2c, the p–n heterojunction formed between ZIF-67 and $LaFeO_3$ was employed as an effective photocatalyst, which provides a clear illustration of the electron transport and the photocatalytic reaction mechanism. The p-type semiconductor $LaFeO_3$ has a Fermi level at the VB, while the n-type semiconductor ZIF-67 has a Fermi level near the CB. Upon contact, the more positive valence band of ZIF-67 and the more negative conduction band of $LaFeO_3$ establish a potential difference, which encourages directional charge transfer across the heterojunction and boosts photocatalytic activity. The ZIF-67/$LaFeO_3$ composite establishes a direct Z-scheme heterojunction, by the synergistic coupling of their electronic band

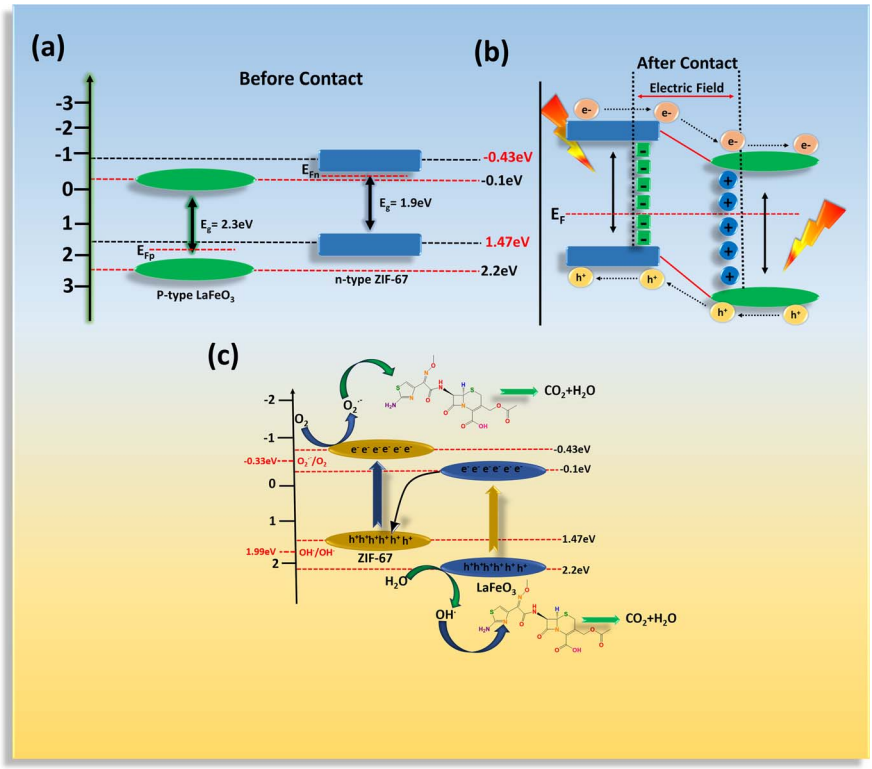

Scheme 2 Schematic diagrams for energy bands of n-ZIF-67 and p-$LaFeO_3$: (a) before contact and (b) after the formation of the p–n heterojunction, and (c) the photocatalytic mechanism on the ZIF-67/$LaFeO_3$ composite.

structure and interfacial charge transfer characteristics. Based on the estimated band edge positions, $LaFeO_3$ posseses a relatively less negative conduction band (CB) and a more positive valence band (VB), whereas ZIF-67 exhibits a more negative CB potential. Upon photoexcitation, both components generate electron–hole pairs, however driven by the internal electric field and band potential difference, the photogenerated electrons in the CB of $LaFeO_3$ preferentially recombine with holes in the VB of ZIF-67 at the interface.[72] This charge recombination pathway confirms the formation of a direct Z-scheme rather than a conventional type-II heterojunction. Consequently electrons with strong reduction potential are retained in the CB of ZIF-67, while holes with strong oxidation potential remain in the VB of $LaFeO_3$, thereby maximizing the redox capability of the system. Since the CB of ZIF-67 is more negative than the reduction potential of $O_2/O_2^{\cdot-}$ (−0.33 *vs.* NHE), these electrons then combine with dissolved molecular oxygen to produce superoxide radicals ($O_2^{\cdot-}$).[73] Whereas the holes in $LaFeO_3$ subsequently react with H_2O to generate hydroxyl radicals, as the hydroxyl radical formation potential (1.99 *vs.* NHE)[74] is lower than the valence band of $LaFeO_3$. The overall photo-Fenton CFX degradation process is outlined below.

$$\text{ZIF-67/LaFeO}_3 + h\nu \rightarrow e_{CB}^- + h_{VB}^+ \quad (34)$$

$$e_{CB}^- + O_2 \rightarrow O_2^{\cdot-} \quad (35)$$

$$OH^- + h_{VB}^+ \rightarrow OH^{\cdot} \quad (36)$$

$$Fe^{3+} + e_{CB}^- \rightarrow Fe^{2+} \quad (37)$$

$$Fe^{2+} + H_2O_2 \rightarrow Fe^{3+} + OH^{\cdot} + OH^- \quad (38)$$

$$Fe^{3+} + H_2O_2 \rightarrow Fe^{2+} + HO_2^{\cdot} + H^+ \quad (39)$$

$$O_2^{\cdot-} + H_2O_2 + (Fe^{3+}/Fe^{2+}) \rightarrow OH^{\cdot} + OH^- + O_2 \quad (40)$$

$$OH^{\cdot} + \text{CFX} \rightarrow CO_2 + H_2O + \text{degraded products} \quad (41)$$

$$O_2^{\cdot-} + \text{CFX} \rightarrow CO_2 + H_2O + \text{degraded products} \quad (42)$$

6. Identification of intermediates and the proposed degradation mechanism

The High-Resolution Mass Spectroscopy (HRMS) study of CFX degradation using ZIF-67/$LaFeO_3$ under xenon lamp irradiation highlights effective photocatalysis. The absence of the parent ion ($m/z = 455$, $[M^+H]^+$) of CFX suggests strong adsorption onto the catalyst or ionization suppression. This analysis was conducted using a Waters XEVO-G2XS QTOF mass spectrometer, featuring an electrospray ionization (ESI) source in positive mode, and was performed using the degradation product to identify the formed intermediates and elucidate their nature. Based on structural analysis, CFX may be separated into three major substructures, denoted A, B, and C, as seen in Fig. 16. The

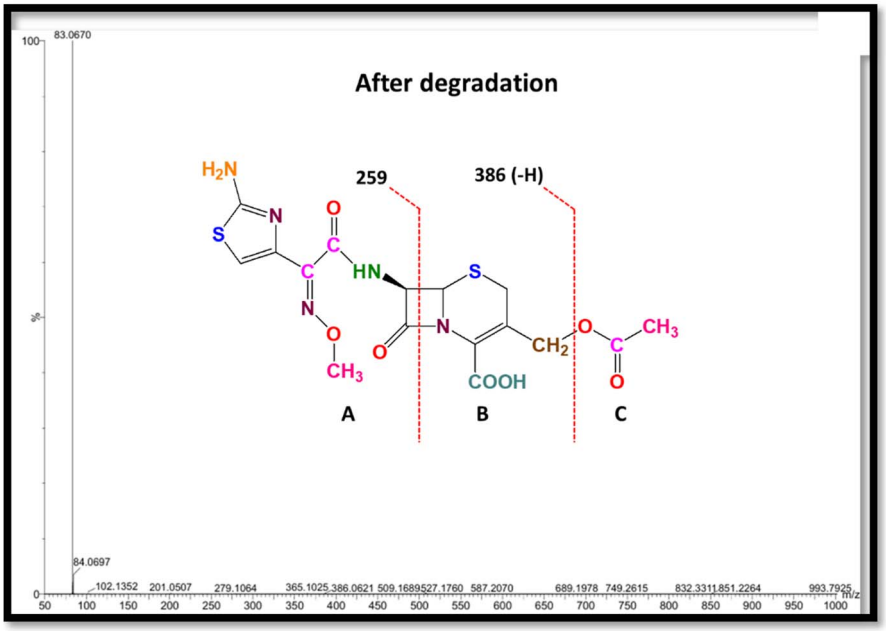

Fig. 16 High-Resolution Mass Spectroscopy (HRMS) analysis of CFX using ZIF-67/$LaFeO_3$.

primary molecular framework is represented by substructure B, the ion identified at *m*/*z* 259 is related to substructure A, and the acetyl group is connected to the methyl group at the 3-position of the cepham core by structure C. The combined mass spectra of deacetyl and deacetoxy CFX show that the β-lactam ring fragments, and deacetyl CFX experiences allylic cleavage, which results in the loss of a water molecule. The detailed pathway of intermediate products during CFX degradation using ZIF-67/$LaFeO_3$, after 10 minutes of reaction, is illustrated Fig. 17. An allylic cleavage process involving the loss of the acetyl group connected to the methyl substituent at the 3-position of the cephem nucleus is responsible for the main ion at *m*/*z* 365. The intermediate produced at *m*/*z* 279 by the second fragmentation, which is characteristics of β-lactam ring rupture, is 2-(2-aminothiazol-4-yl)-2(methoxyimino)-*N*-(2-oxoethyl)acetamide. This molecule also undergoes the loss of an acetaldehyde unit, leading to the formation of 2-(2-aminothiazol-4-yl)-2(methoxyimino)acetamide, which is identified at *m*/*z* 201. This molecule also loses an acetaldehyde unit. Additionally, this results in the production of *m*/*z* 102 and *m*/*z* 100, which correspond to the loss of the five membered ring containing the main amine and oxime functional groups. The intermediate products would eventually breakdown into tiny inorganic components (Table S7).

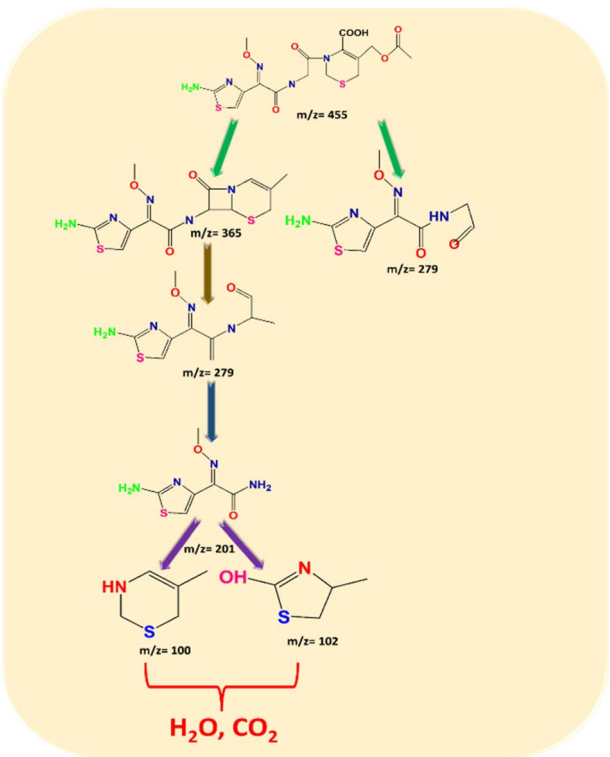

Fig. 17 High-Resolution Mass Spectroscopy (HRMS) sequential breakdown process of cefotaxime degradation using the ZIF-67/$LaFeO_3$ composite.

7. Ecotoxicity assessment

To evaluate the potential for practical catalytic applications, it is important to investigate the ecotoxicity of CFX degradation intermediaries. Although Fenton-based processes are highly effective for antibiotic degradation, they are often associated with the formation of transformation products that can exhibit equal or even greater toxicity than the parent compound.[75–77] Wastewater discharged from aquaculture, medical, and agricultural activities contains a wide range of antibiotic residues, with the agricultural sector exerting significant environmental impact. To assess the ecotoxicity of CFX and its degradation products, wheat (*Triticum aestivum*), a commonly cultivated

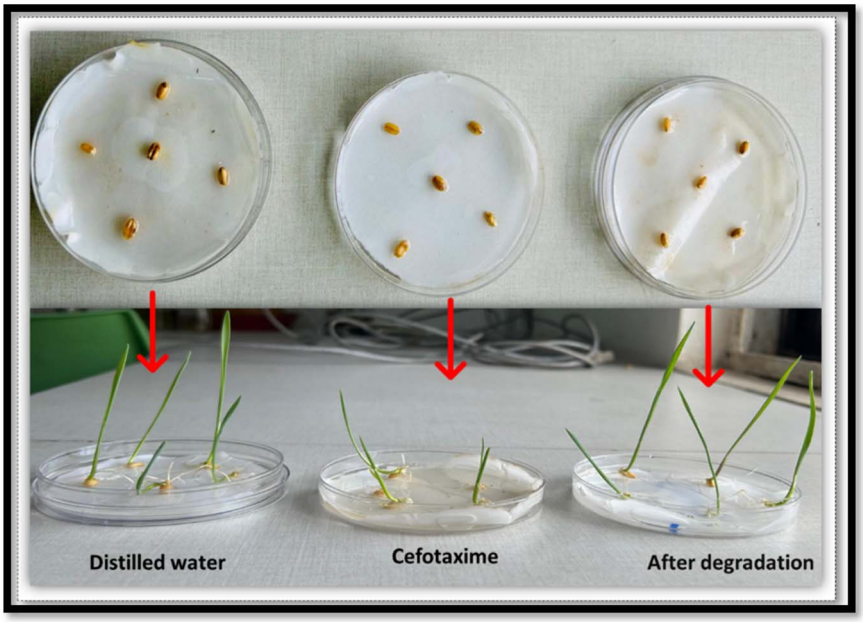

Fig. 18 Effects of different CFX solutions on the growth of wheat.

crop plant, was selected for a five-day germination assay. The growth profiles of wheat seedlings on days 1 and 5 under three different conditions—pure water (control), untreated CFX (20 mg L^{-1}), and photo catalytically degraded CFX (20 mg L^{-1})—are shown in Fig. 18. In contrast to CFX, which results in poor or stunted germination with shorter and fewer shoots, seeds grown in pure water exhibit vigorous, healthy germination with tall green shoots. Notably, seeds grown in degraded CFX, showed significantly improved germination and growth, comparable to or approaching that of the control group, indicating a substantial reduction in toxicity. The control results confirm that the seeds possessed normal germination potential. These findings demonstrate that CFX clearly inhibits seed development, whereas its photocatalytic degradation products exhibit markedly lower ecotoxicity. The successful remediation of degraded CFX suggests that biodegradation may be a practical way to purify antibiotic-contaminated environments. It is hypothesized that photocatalytic degradation converts CFX into smaller, less toxic inorganic or low-molecular-weight compounds that are more compatible with plant growth. Overall, the results indicate a significant improvement in the water quality following CFX degradation (20 mg L^{-1}) using the ZIF-67/$LaFeO_3$ composite catalyst.

8. Conclusion

This study demonstrates the successful engineering of a ZIF-67/$LaFeO_3$ composite featuring a type-II p–n heterojunction that enables efficient charge-transfer pathways for multiple functionalities, including antibiotic sensing, ecotoxicity assessment of CFX and its degradation intermediaries using seed–water culture assays, and highly effective photo-Fenton degradation under visible-light irradiation with excellent photostability. In the absence of H_2O_2, the photocatalytic degradation of CFX achieved an efficiency of 83.1% within 75 minutes. The degrading efficiency, however, dramatically increased to 90.1% in just 10 minutes after adding H_2O_2 to the system. This significant improvement highlights the vital function of H_2O_2 as an electron acceptor, which speeds up the production of reactive oxygen species and significantly increases the rates at which CFX degrades. The enhanced photocatalytic and photo-Fenton performance is attributed to the formation of a type-II p–n heterojunction, which provides strong redox potential energy bands, broad visible-light absorption, and efficient charge separation and transfer. Furthermore, the synergistic effects of interfacial charge transfer across the type-II p–n heterojunction and the rapid Fe^{3+}/Fe^{2+} cycling promotes the continuous generation of reactive oxygen species, leading to outstanding photo-Fenton activity. High-resolution mass spectrometry (HR-MS) analysis identified six intermediate products, enabling the proposal of two plausible CFX degradation pathways and offering deeper insight into the transformation behaviour and degradation mechanism of CFX during the photocatalytic process. In addition to its degradation capability, the ZIF-67/$LaFeO_3$ composite-modified screen-printed carbon electrode (SPCE) exhibited electrochemical sensing performance toward CFX, highlighting the multifunctional potential of this heterostructure material for environmental monitoring and remediation applications. A limit of quantification (LOQ) of 10.1 ppm and a limit of detection (LOD) of 3.41 ppm/7.5 μM was shown by the sensor. Electrochemical sensing of cefotaxime was explored as a proof-of-concept application to demonstrate the electrocatalytic functionality of the ZIF-67/$LaFeO_3$ hybrid material, rather than as an attempt to develop an optimized analytical sensor. As summarized in Table S6, several electrochemical sensors reported in the literature achieve lower detection limits for β-lactam antibiotics through the use of noble metals, molecular imprinting, or multi-step amplification

strategies. In contrast, the present study does not aim to optimize analytical sensitivity but rather demonstrates the feasibility of utilizing a MOF–perovskite hybrid as an electrocatalytic sensing interface under near-neutral conditions. The observed detection limit of 3.41 ppm is therefore adequate to validate the material's electrochemical functionality and highlights its potential for further sensor optimization. In particular, the suggested work might aid in the design of nano-heterojunctions for environmental remediation applications including wastewater treatment and antibiotic electrochemical detection. Designed for real world applications, the material is recyclable and easily integrated into membrane-based wastewater treatment systems.

Author contributions

Monalisa Samal: conceptualization, writing – original draft, methodology, investigation and data curation. Dakshita Snud Sharma: methodology and data curation. Dharitri Rath: formal analysis, conceptualization, validation, and visualization. P. Ganga Raju Achary: formal analysis, validation, and editing. Jagannath Panda: data curation and formal analysis. Binita Nanda: supervision, conceptualization, validation, review and editing.

Conflicts of interest

All authors are equally contributed to the processing of article. There is no conflict of interest among all the authors.

Data availability

All data and materials are included in the manuscript.

Supplementary information (SI) is available. See DOI: https://doi.org/10.1039/d6na00081a.

Acknowledgements

All authors are thankful to SOA 'Deemed' to be University for its constant support throughout this research work.

References

1 R. L. P. Rocha, A. Í. S. Morais, F. P. Araujo, L. M. C. Honório, M. P. Silva, M. B. Furtini, E. G. Vieira, E. C. da Silva-Filho and J. A. Osajima, *ACS Omega*, 2025, **10**(6), 5351–5361.
2 J. Sun, C. Jiang, Z. Wu, Y. Liu and S. Sun, *Chemosphere*, 2022, **308**, 136107.
3 R. L. P. Rocha, L. M. C. Honorio, R. D. d. S. Bezerra, P. Trigueiro, T. M. Duarte, M. G. Fonseca, E. C. Silva-Filho and J. A. Osajima, *Minerals*, 2022, **12**, 525.
4 S. Zheng, Y. Xu, X. Yao, C. Wang, P. Liu, H. Zhao, J. Lu and J. Ju, *Separations*, 2024, **11**, 63.
5 N. F. F. Moreira, J. M. Sousa, G. Macedo, A. R. Ribeiro, L. Barreiros, M. Pedrosa, J. L. Faria, M. F. R. Pereira, S. Castro-Silva, M. A. Segundo, *et al.*, *Water Res.*, 2016, **94**, 10–22.
6 F. Wang, Y. Feng, P. Chen, Y. Wang, Y. Su, Q. Zhang, Y. Zeng, Z. Xie, H. Liu, Y. Liu, *et al.*, *Appl. Catal., B*, 2018, **227**, 114–122.
7 S. O. Ganiyu, M. Zhou and C. A. Mart\'\inez-Huitle, *Appl. Catal., B*, 2018, **235**, 103–129.
8 A. M. Chávez, O. Gimeno, A. Rey, G. Pliego, A. L. Oropesa, P. M. Álvarez and F. J. Beltrán, *Chem. Eng. J.*, 2019, **361**, 89–98.
9 J. Luo, S. Zhang, M. Sun, L. Yang, S. Luo and J. C. Crittenden, *ACS Nano*, 2019, **13**, 9811–9840.
10 Z. Yang, C. Shan, J. J. Pignatello and B. Pan, *Environ. Sci. Technol.*, 2022, **56**, 6621–6630.
11 M. Imran, A. Z. Abdullah, M. E. Khan and A. Mohammad, *J. Environ. Manage.*, 2025, **373**, 123759.
12 M. Moradi, A. Elahinia, Y. Vasseghian, E.-N. Dragoi, F. Omidi and A. M. Khaneghah, *J. Environ. Chem. Eng.*, 2020, **8**, 104330.
13 M. Imran, A. Z. Abdullah, M. Arishi, S. K. Ali, M. E. Khan, M. Fellah and A. A. Chaudhary, *Ceram. Int.*, 2025, **51**(25), 44598–44611.
14 M. Imran, A. Z. Abdullah, M. E. Khan, Y.-M. Kim and F. Khan, *J. Taiwan Inst. Chem. Eng.*, 2025, **171**, 106068.
15 A. Khan, S. Sadiq, I. Khan, M. Humayun, G. Jiyuan, M. Usman, A. Khan, S. Khan, A. F. Alanazi and M. Bououdina, *Heliyon*, 2024, **10**(5), e27378.
16 K. S. Park, Z. Ni, A. P. Côté, J. Y. Choi, R. Huang, F. J. Uribe-Romo, H. K. Chae, M. O'Keeffe and O. M. Yaghi, *Proc. Natl. Acad. Sci. U. S. A.*, 2006, **103**, 10186–10191.
17 M. Zhang, Q. Shang, Y. Wan, Q. Cheng, G. Liao and Z. Pan, *Appl. Catal., B*, 2019, **241**, 149–158.
18 K. G. M. Laurier, F. Vermoortele, R. Ameloot, D. E. De Vos, J. Hofkens and M. B. J. Roeffaers, *J. Am. Chem. Soc.*, 2013, **135**, 14488–14491.
19 W. Liang, H. Xu, F. Carraro, N. K. Maddigan, Q. Li, S. G. Bell, D. M. Huang, A. Tarzia, M. B. Solomon, H. Amenitsch, *et al.*, *J. Am. Chem. Soc.*, 2019, **141**, 2348–2355.
20 N. Askari, M. Beheshti, D. Mowla and M. Farhadian, *Chemosphere*, 2020, **251**, 126453.
21 K. Wang, H. Niu, J. Chen, J. Song, C. Mao, S. Zhang and Y. Gao, *Appl. Surf. Sci.*, 2017, **404**, 138–145.
22 H. Tanaka, *Catal. Surv. Asia*, 2005, **9**, 63–74.
23 M. A. Peña and J. L. G. Fierro, *Chem. Rev.*, 2001, **101**, 1981–2018.
24 M. Imran, S. Ahmed, A. Z. Abdullah, J. Hakami, A. A. Chaudhary, H. A. Rudayni, S.-U.-D. Khan, A. Khan and N. S. Basher, *Luminescence*, 2023, **38**, 1064–1086.
25 N. Sobahi, M. Imran, M. E. Khan, A. Mohammad, M. M. Alam, T. Yoon, I. M. Mehedi, M. A. Hussain, M. J. Abdulaal and A. A. Jiman, *Materials*, 2023, **16**, 2770.
26 H. A. Alhazmi, M. Imran, S. Ahmed, M. Albratty, H. A. Makeen, A. Najmi and M. S. Alam, *Phys. Scr.*, 2023, **98**, 105006.
27 M. Soleymani, A. Moheb and D. Babakhani, *Chem. Eng. Technol.*, 2011, **34**, 49–55.
28 H. Falcon, R. E. Carbonio and J. L. G. Fierro, *J. Catal.*, 2001, **203**, 264–272.
29 H. Gong, X. Zhang, G. Wang, Y. Liu, Y. Li and Z. Jin, *Mol. Catal.*, 2020, **485**, 110832.
30 Y. Li, Z. Jin and T. Zhao, *Chem. Eng. J.*, 2020, **382**, 123051.

31 S. N. Tijare, M. V Joshi, P. S. Padole, P. A. Mangrulkar, S. S. Rayalu and N. K. Labhsetwar, *Int. J. Hydrogen Energy*, 2012, **37**, 10451–10456.
32 A. Boulahouache, M. Benlembarek, N. Salhi, A. M. Djaballah, C. Rabia and M. Trari, *Int. J. Hydrogen Energy*, 2023, **48**, 14650–14658.
33 G. Iervolino, V. Vaiano, D. Sannino, L. Rizzo and V. Palma, *Appl. Catal., B*, 2017, **207**, 182–194.
34 N. Entezami, M. Farhadian, A. R. S. Nazar and S. Tangestaninejad, *Process Saf. Environ. Prot.*, 2022, **164**, 747–760.
35 Y. Wang, J. Xu, G. Sheng, J. Wang, B. Yang, H. Jiang, N. Liu and X. Zhang, *Sep. Purif. Technol.*, 2025, **362**, 4981295.
36 N. Askari, M. Beheshti, D. Mowla and M. Farhadian, *J. Photochem. Photobiol., A*, 2020, **394**, 112463.
37 P. Nunocha, M. Kaewpanha, T. Bongkarn, A. Phuruangrat and T. Suriwong, *Mater. Sci. Semicond. Process.*, 2021, **134**, 106001.
38 M. Afkhami-Ardekani, M. R. Naimi-Jamal, S. Doaee and S. Rostamnia, *Catalysts*, 2022, **13**, 9.
39 N. Sharma, H. S. Kushwaha, S. K. Sharma and K. Sachdev, *RSC Adv.*, 2020, **10**, 1297–1308.
40 X. Ren, H. Yang, S. Gen, J. Zhou, T. Yang, X. Zhang, Z. Cheng and S. Sun, *Nanoscale*, 2016, **8**, 752–756.
41 F. Wang, H. Yang and Y. Zhang, *Mater. Sci. Semicond. Process.*, 2018, **73**, 58–66.
42 J. Qin, S. Wang and X. Wang, *Appl. Catal., B*, 2017, **209**, 476–482.
43 V. Pandey, A. Bansal and A. P. Toor, *Environ. Sci. Pollut. Res.*, 2024, **31**, 28578–28593.
44 Q. Zhang, Z. Li, S. Chen, Z. Zhang, S. Ali and L. Jing, *Catal. Today*, 2020, **339**, 403–410.
45 M. Davoodi, F. Davar, M. R. Rezayat, M. T. Jafari, M. Bazarganipour and A. E. Shalan, *RSC Adv.*, 2021, **11**, 13245–13255.
46 H. Jalili, B. Aslibeiki, A. G. Varzaneh and V. A. Chernenko, *Beilstein J. Nanotechnol.*, 2019, **10**, 1348–1359.
47 M. Imran, A. Z. Abdullah, M. S. Rashid, O. Y. Bakather, A. M. Alshoaibi, M. E. Khan, S. K. Ali and A. A. Chaudhary, *Inorg. Chem. Commun.*, 2025, 115681.
48 A. E. Giannakas, A. K. Ladavos and P. J. Pomonis, *Appl. Catal., B*, 2004, **49**, 147–158.
49 A. Barjola, J. Escorihuela, A. Andrio, E. Giménez and V. Compañ, *Nanomaterials*, 2018, **8**, 1042.
50 N. Karami, F. Davar and S. Hasani, *Mater. Res. Express*, 2019, **6**, 95092.
51 Q. Yang, S. Ren, Q. Zhao, R. Lu, C. Hang, Z. Chen and H. Zheng, *Chem. Eng. J.*, 2018, **333**, 49–57.
52 V. Guigoz, L. Balan, A. Aboulaich, R. Schneider and T. Gries, *Int. J. Hydrogen Energy*, 2020, **45**, 17468–17479.
53 G. M. Bancroft, H. W. Nesbitt, R. Ho, D. M. Shaw, J. S. Tse and M. C. Biesinger, *Phys. Rev. B: Condens. Matter Mater. Phys.*, 2009, **80**, 75405.
54 Q.-H. Wu, M. Liu and W. Jaegermann, *Mater. Lett.*, 2005, **59**, 1980–1983.
55 D. G. Popescu, N. Barrett, C. Chirila, I. Pasuk and M. A. Husanu, *Phys. Rev. B: Condens. Matter Mater. Phys.*, 2015, **92**, 235442.
56 R. A. Villa-Bustamante, J. A. Jativa, R. Ospina, R. F. Londono-Menjura, J. F. Jurado, J. H. Quintero, E. Restrepo-Parra and A. Mello, *Eng. Sci.*, 2018, **11**, 4021–4039.
57 N. Gunasekaran, S. Rajadurai, J. J. Carberry, N. Bakshi and C. B. Alcock, *Solid State Ionics*, 1994, **73**, 289–295.
58 T. M. Al-Shahumi, I. A. Al-Omari, S. H. Al-Harthi and M. T. Z. Myint, *SN Appl. Sci.*, 2023, **5**, 121.
59 V. R. Mastelaro, P. N. Lisboa-Filho, P. P. Neves, W. H. Schreiner, P. A. P. Nascente and J. A. Eiras, *J. Electron Spectrosc. Relat. Phenom.*, 2007, **156**, 476–481.
60 J. Wang, Z. Yu, T. Zhao, Y. Song, H. Liu, J. Hou and P. Yu, *Appl. Surf. Sci.*, 2025, 163837.
61 W. S. Hummers Jr and R. E. Offeman, *J. Am. Chem. Soc.*, 1958, **80**, 1339.
62 Q. Li, Q. Zhou, H. Deng, Z. Li, B. Xue, A. Liu, B. Shen, D. Hao, H. Zhu and Q. Wang, *Appl. Catal. B Environ. Energy*, 2025, **360**, 124533.
63 X. Liu, Y. Gong, H. M. Azharul, G. Wang, X. Zhang, D. Sun, H. Ma, *et al.*, *Water, Air, Soil Pollut.*, 2025, **236**, 1–16.
64 J. Li, W. Guan, X. Yan, Z. Wu and W. Shi, *Catal. Lett.*, 2018, **148**, 23–29.
65 M. Gumustas and S. A. Ozkan, *Open Anal. Chem. J.*, 2011, **5**, 1–21.
66 V. Van Pham, T. K. Truong, L. V. Hai, H. P. P. La, H. T. Nguyen, V. Q. Lam, H. D. Tong, T. Q. Nguyen, A. Sabbah, K.-H. Chen, *et al.*, *ACS Appl. Nano Mater.*, 2022, **5**, 4506–4514.
67 P. Gholami, A. Khataee, R. D. C. Soltani, L. Dinpazhoh and A. Bhatnagar, *J. Hazard. Mater.*, 2020, **382**, 121070.
68 L. Yang, Y. Xiang, F. Jia, L. Xia, C. Gao, X. Wu, L. Peng, J. Liu and S. Song, *Appl. Catal., B*, 2021, **292**, 120198.
69 F. Niu, D. Chen, L. Qin, N. Zhang, J. Wang, Z. Chen and Y. Huang, *ChemCatChem*, 2015, **7**, 3279–3289.
70 S. Nazari, E. Asgari, A. Sheikhmohammadi, S. A. Mokhtari and H. Alamgholiloo, *J. Environ. Chem. Eng.*, 2023, **11**, 110393.
71 Y. Song, S. Xue, G. Wang, J. Jin, Q. Liang, Z. Li and S. Xu, *J. Phys. Chem. Solids*, 2018, **121**, 329–338.
72 Y. Zhang, Z. Jin, H. Yuan, G. Wang and B. Ma, *Appl. Surf. Sci.*, 2018, **462**, 213–225.
73 P. Xia, B. Zhu, B. Cheng, J. Yu and J. Xu, *ACS Sustainable Chem. Eng.*, 2018, **6**, 965–973.
74 P. Priyadarshini, A. Mishra, A. Majhi, K. Parida and K. Parida, *ACS Appl. Energy Mater.*, 2025, **8**, 5067–5081.
75 Q. Li, B. Xue, Z. Wang, H. Zhu, H. Zhou, H. Deng, J. Song, X. Ma, H. Du, Q. Wang, *et al.*, *Sep. Purif. Technol.*, 2024, **338**, 126450.
76 O. González, C. Sans and S. Esplugas, *J. Hazard. Mater.*, 2007, **146**, 459–464.
77 A. G. Trovo, R. F. P. Nogueira, A. Agüera, A. R. Fernandez-Alba and S. Malato, *Water Res.*, 2011, **45**, 1394–1402.